Experimental validation of CLEAN-SC for the determination of directivity of engine noise sources

Jared Vermeulen

TUDelft

Delft
University of
Technology

Experimental validation of CLEAN-SC for the determination of directivity of engine noise sources

Thesis report

by

Jared Vermeulen

to obtain the degree of Master of Science
at the Delft University of Technology
to be defended publicly on August 6, 2024

Thesis committee:
Chair:	Dr.ir. Mirjam Snellen
Supervisors:	Dr. Roberto Merino-Martínez
	Dr.ir. Pieter Sijtsma
External examiner:	Dr. ir. Tomas Sinnige
Place:	Faculty of Aerospace Engineering, Delft
Project Duration:	November, 2023 - June, 2024
Student number:	4809467

An electronic version of this thesis is available at http://repository.tudelft.nl/.

Faculty of Aerospace Engineering · Delft University of Technology

TUDelft Delft University of Technology

Preface

This master thesis investigates the capability of CLEAN-SC to separate the noise of different aero-engine components, including their individual directivity. Aircraft and turbofan noise is a relevant issue. In addition CLEAN-SC is one of the most commonly used algorithms for processing microphone array data. This combination makes this study in my opinion an interesting research topic.

The main aim of this study is to determine how precise the breakdown of the noise is using CLEAN-SC. So that this feature of CLEAN-SC can be applied to microphone data of static engine tests or possibly other applications. The validation of the breakdown capability of CLEAN-SC is performed using experimental data, which is obtained through tests. These experiments are one of the highlights of this thesis, and I am thankful for the opportunity to conduct real tests. I would like to extend my gratitude to Amy Morin for her invaluable assistance with all the equipment and the setup of the tests.

Additionally, I am grateful to my main supervisor, Roberto Merino-Martínez, for his guidance and support throughout the project. I would also like to thank my other supervisor, Pieter Sijtsma, for his help and great expertise in the field. Finally, I extend my thanks to Mirjam Snellen for her insightful advice.

Summary

With the increasing number of aircraft and the increasing number of people living near airports, noise pollution caused by aircraft is expected to increase. The engines are the single largest noise source of modern aircraft. Noise radiation from the engine is highly directional and it is, therefore, important to be able to obtain this directivity from microphone data from static engine tests. So that the noise of specific components can be decreased.

Currently, in static engine testing the most common ways to process microphone array data are conventional frequency domain beamforming (CFDBF) [1] and integration methods [2] [3]. These methods are applied to the microphone array data to obtain average level breakdown. This means that the average level of the microphone array is written as a summation over the different sources. However, using those methods the directivity and level of the individual components remains unknown [4].

There are tools that can perform the breakdown into components including directivity, such as SODIX [5] and AFINDS [6]. These tools rely on inverse methods, which makes the implementation of such tools not straightforward. An alternative method has been proposed by Sijtsma, which is to use CLEAN-SC [7] to process array data of static engine tests to include directivity of individual components. The implementation of CLEAN-SC is more straightforward and requires less computation time compared to the other methods. Subsequently, it has been demonstrated that CLEAN-SC is capable of such a breakdown of microphone data of a static engine test of a DGEN380 turbofan engine [4]. The directivity results are plausible, but further validation that CLEAN-SC is capable of performing a directivity breakdown is required.

The validation of this capability of CLEAN-SC is performed by the analysis microphone data of a well-controlled experiment, in which the location and directivity of the sources is known. This way the accuracy of the directivity breakdown using CLEAN-SC can be determined, by comparing directivity of one source to the same source, when multiple sources are present. The experiment itself consists of cylindrical aluminum pipe with two speakers inside, to resemble a turbofan engine. Moreover, each speaker faces a different exit of the pipe and can be controlled individually. Tests are performed with and without an insulating layer of acoustic foam in between the speakers. The foam prevents leakage of sound from one exit of the pipe to the other, which allows the sources to be isolated. In addition tests are performed for two pipes of different diameters. The experiments are performed in an anechoic chamber to minimize background noise and reflections.

The data in the experiment is recorded using a 52 equidistant microphone array. The array data is analysed by making acoustic source maps using three methods; conventional frequency domain beamforming (CFDBF), DAMAS and CLEAN-SC. The source maps show the effect of the layer of acoustic foam. Moreover, these maps also show how different beamforming methods affect the quality of the source maps and the number of grating lobes that are visible in the maps. Moreover, the acoustic maps from CLEAN-SC show that almost all sources are located at the exits of the pipe, except for some grating lobes. Furthermore, CLEAN-SC is used to perform directivity breakdown of the microphone data of the experiments. The directivity breakdowns are compared to determine the precision of the breakdown capability of CLEAN-SC. In addition a root mean square analysis is applied to obtain a better overview over a frequency range.

The results show that the accuracy of the breakdown of a component is high, around 0.5 dB when the analysed component is the dominant source in the spectrum. If the analysed source is only a small fraction of the total noise, the accuracy of the breakdown of that component decreases to around 2 dB. When the analysed component is one of the dominant sources the accuracy is around 1 dB in the directivity breakdown. So based on the results of this study, CLEAN-SC should be able to reliably perform directivity breakdown of microphone data of static engine tests, especially for the areas where the noise of the analysed part is either the dominant source or one of the dominant sources.

Nomenclature

Latin Symbols	
A	source power
a	radius of a duct
B	number of blades
c_0	speed of sound
C	Cross-spectral matrix
D	degraded CSM
f	frequency
$g_{j,n}$	steering vector for grid point j and microphone n
h_j	Source component for grid point j
i	imaginary unit
J	number of grid points
$j_{m,\mu}$	zeros of the Bessel functions
K	number of sources
$\dot{m}$	mass flow
N_{mic}	number of microphones
n_{rot}	rotations per minute
$\mathbf{p}$	vector containing pressure amplitudes per microphone
R_1	distance from source to furthest microphone
R_2	distance from source to closest microphone
T	thrust
v_∞	speed of aircraft
v_j	exhaust velocity
$\mathbf{w_j}$	weighted steering vector
$\mathbf{x}$	equivalent source distribution
$\mathbf{x_n}$	vector of microphone positions
X	x-location in grid
$\mathbf{y}$	source power output

Greek Symbols	
Δt	time delay
η_j	propulsive efficiency
ϕ	loop gain
ξ_j	scan point

Subscripts	
bypass	area corresponding to the bypass
core	area corresponding to the core
c	cut-off frequency
intake	referring to the intake of the engine
j	j^{th} grid point
jet	reffering to a jet exhaust
k	k^{th} source
left	referring to left exit
m	m^{th} root of the Bessel function
max	maximum
mic	microphone
n	n^{th} microphone
other	referring to area, that is not left or right
right	referring to right exit
rot	rotational
μ	order of the Bessel function
∞	free stream conditions

Superscripts	
L	l^{th} iteration
*	complex conjugate transpose

Contents

1

Introduction

Over the next 20 years global aviation is expected to grow annually by 3.6% [8]. After a dip during the pandemic the global market has recovered rapidly [9], as depicted in Fig. 1.1. As a consequence the noise pollution caused by aviation will increase, if no significant improvements are made. Especially because airports are located near densely populated areas and big cities [10]. This means that in the future more people can be affected by noise pollution due to aircraft. Continuous exposure to aircraft noise pollution is shown to be detrimental for human health, with increased risk for ailments such as high blood pressure, depression and stress [11]. In addition it has also been shown that aircraft noise can lead to significant sleep disruption [12]. Subsequently, regulations with regards noise pollution in general are becoming more strict [13]. This makes aircraft noise an important and relevant issue to investigate.
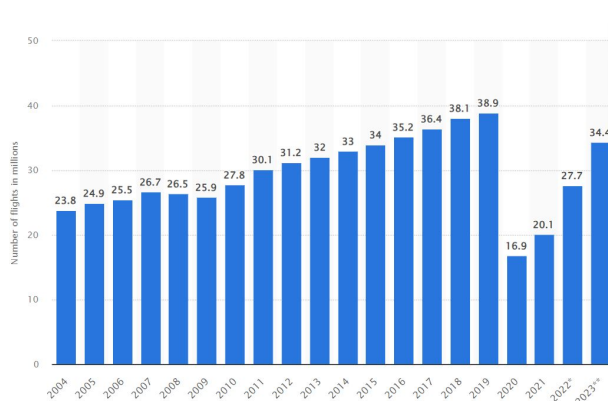

Figure 1.1: Total number of annual flights in millions from [14]. * indicates an estimate and ** indicates forecast

The main noise sources of an aircraft can be broken down into two categories the airframe and the engines [15] [16]. Airframe noise consists of the airflow interacting with the high lift devices, the wings, the landing gear or a combination. The airframe noise is dominant or on par with the engine noise during the approach phase [17]. While engine noise is the primary source during take-off. An example of a breakdown of the noise of an Airbus A319 during approach is shown in Fig. 1.2a and departure in Fig. 1.2b. Hence, the engines form a large part of the annoyance caused by aircraft and therefore, the focus of this study is on engine noise. More specifically turbofan engines, since these are the most used type of engines on modern aircraft. In addition this study focuses on how to breakdown the noise of a turbofan engine from microphone data of a static engine test.
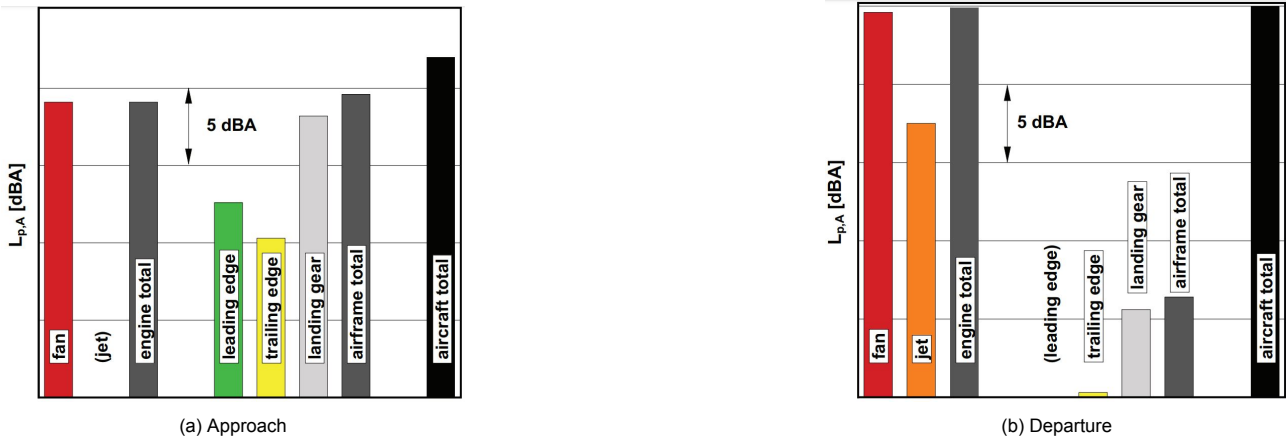
1

Figure 1.2: Breakdown of the estimated noise of an A319 aircraft from an observer on the ground in $L_{p,A}$ adapted from [15]

The noise generated by a turbofan engine can be split up into different parts. In general a distinction is made between core, jet, fan and compressor noise, the underlying mechanisms will be discussed in more detail in chapter 2. Subsequently, the noise radiating of these parts is highly directive. The noise observed in the far field is dependent on the location with respect to the engine, which makes this useful information to obtain about a turbofan engine. Currently, information about the noise of an engine is obtained in static engine tests. In these tests the engine is put on a test bed, inside of an anechoic dome. Next, the engine is turned on and the microphone array above records the noise of the engine for different engine settings. In Fig. 1.3, such a test is shown for a DGEN380 turbofan engine inside the NASA Glenn Aero-acoustic Propulsion Laboratory anechoic dome [18].
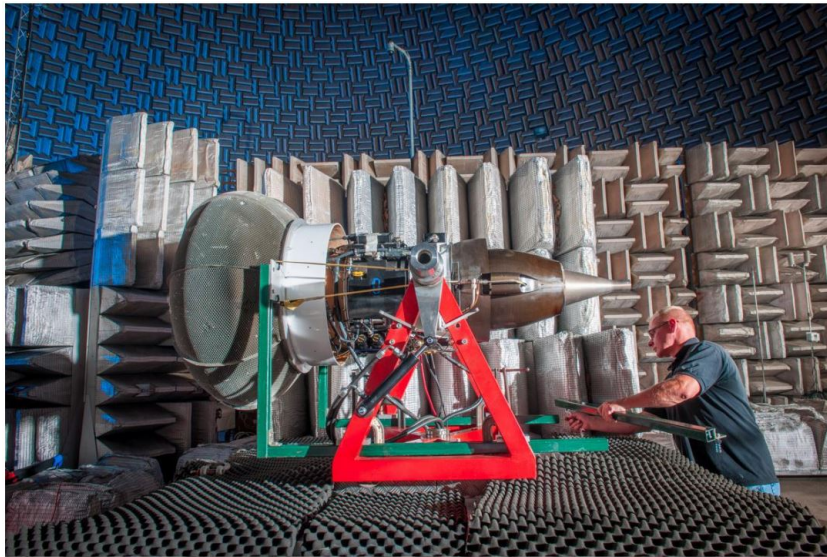

Figure 1.3: Static engine test of a DGEN380 turbofan engine inside the NASA Glenn Aero-Acoustic Propulsion Laboratory anechoic dome [18]

The next step is to process the data of the microphone array of the tests. The most common ways to process microphone array data are conventional frequency domain beamforming (CFDBF) [1] and integration methods [2] but there are many more methods to process acoustic microphone data with varying accuracy and processing time [3]. These methods are applied to the microphone array data to obtain average level breakdown. This means that the average level of the microphone array is written as a summation over the different sources. However, using those methods the directivity of the individual sources remains unknown [4].

There are tools that can perform the breakdown including directivity, such as SODIX [5] and AFINDS [6]. These tools rely on inverse methods, which makes the implementation of such tools not straightforward. An alternative method has been proposed by Sijtsma, which is to use CLEAN-SC [7] to process array data of static engine tests to include directivity. The implementation of CLEAN-SC is more straightforward and requires less computation time compared to the other methods. Subsequently, it has been demonstrated that CLEAN-SC is capable of such a breakdown of test data of DGEN380 engine [4]. The directivity results are plausible, but further validation that CLEAN-SC is capable of performing a directivity breakdown is required. Hence, a well-controlled experiment to validate this capability of CLEAN-SC is performed. Therefore, the goal of this study is to determine the precision of the directivity breakdown of CLEAN-SC.

This study has the following structure. In order to have a better understanding of turbofan engine noise, chapter 2 splits the engine noise into its main components and for each component the main mechanisms that generate noise are discussed. With a better understanding of the underlying mechanisms the research questions are presented in chapter 3. Subsequently, the methods to answer the research questions are explained, which includes the experimental setup and the tools that are applied to analyse the data. In chapter 4, the results of the experiments are presented in the form of acoustic source maps and directivity breakdowns. In addition the directivity breakdowns are investigated in more detail to determine the precision of the breakdown. Finally, in chapter 5, the conclusions of the study are presented.

<div align="right">

2

</div>

<div align="right">

Engine Noise

</div>

This chapter briefly explains how turbojet and turbofan engines work in section 2.1, so that the noise mechanisms can be broken down per part of the engine. The noise mechanisms are split up in core noise section 2.2, jet noise section 2.3 and fan noise section 2.4. Finally an overview of the directionality of the noise radiating from the parts is presented in section 2.5

2.1. Turbojet and Turbofan

Turbojets are the first turbine engines used on aircraft [19]. They work by drawing in air and compressing it, then fuel is added and burned. Leading to a hot compressed mixture of gas, which expands out of the rear of the engine, propelling the aircraft forward. To complete this process conventional turbojets consist of three main stages; a compression stage, a combustion stage and a turbine stage. The compression stage consists of a compressor and an inlet, as shown in Fig. 2.1. Here, the air is directed into the compressor and compressed. The combustor stage is where the fuel is injected and burned, so that the energy of the compressed air is increased due to the increase in temperature. Afterwards, the hot gas passes through the turbine, which removes some energy from the flow to drive the compressor. The turbine and the compressor are connected by the shaft. After passing through the turbine the gas enters the nozzle. The goal of the nozzle is to convert the remaining energy in the gas into velocity, such that it produces thrust. The gas expands until it reaches the freestream pressure, resulting in thrust and then exits back into the ambient.
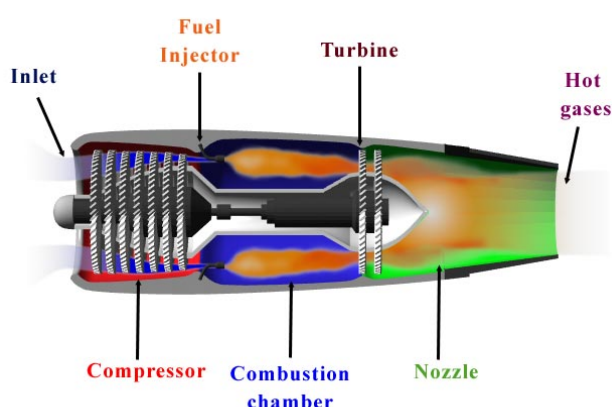

Figure 2.1: Schematic of a turbojet engine [20]

In the 1960s the turbofan was introduced for commercial aircraft [19]. The turbofan is a variation of the turbo-

jet, the main difference concerns the addition of a fan at the front of the engine, which is powered by another turbine stage. This leads to a so-called "twin-spool" engine, as it has two shafts, as shown in Fig. 2.2. The high pressure turbine drives the high pressure compressor and the low pressure turbine drives both the fan and the low pressure compressor. The addition of the fan allows for air to bypass the core of the engine. In modern engines the ratio of air going through the bypass compared to core is around 12:1. As a result a large portion of the thrust is created by the bypass air. The main advantage of the turbofan over the turbojet is the decrease in fuel consumption for the same thrust, due to a higher propulsive efficiency. The propulsive efficiency is given by Eq. (2.1), where v_{jet} is the exhaust velocity and v_0 is the speed of the aircraft. So to obtain a high propulsive efficiency it is beneficial to have v_j close to v_∞, however this does come at the cost of thrust (T), Eq. (2.2), unless the mass flow ($\dot{m}$) increases. Thus for optimal fuel efficiency it is best to accelerate a large portion of air by a small increment. Therefore, the current trend is to increase the fan diameter and bypass ratio to improve efficiency [21].
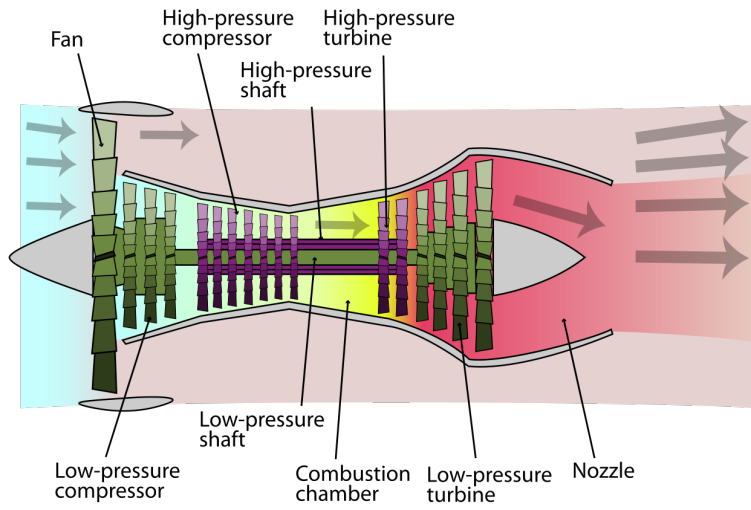

Figure 2.2: Schematic of a turbofan engine [22]

$$\eta_{jet} = \frac{2}{1 + \frac{v_{jet}}{v_\infty}} \qquad (2.1)$$

$$T = \dot{m}(v_{jet} - v_\infty) \qquad (2.2)$$

The noise main sources of a turbofan engine are analogues to the stages of the engine. As a result the noise can be broken down into three categories: jet noise, fan noise and core noise, which will be described in the following sections.

2.2. Engine core noise

In general the core noise emissions are not dominant compared to the other sources [3]. However it can become more dominant in the future as the noise of other main components is reduced. The noise coming from the engine core can be split into two components combustor noise and turbine and compressor noise.

2.2.1. Combustor noise

Combustor noise is generated by the fuel heating process in the combustion chamber [23]. This leads to direct noise due to the expansion of the gas, which produces sound waves through interaction with the surrounding flow. It also leads to indirect noise, caused by the convection of entropy fluctuations from the combustor to the the turbine. The type of noise coming from the combustor is broadband and is mostly coming from the aft of the engine.

2.2.2. Turbine & Compressor noise

Turbine and compressor noise mechanisms are similar to the mechanisms of the fan noise. Tonal noise is generated due to the pressure disturbances by the rotating blades and by the interaction of the rotating wake with the vanes [23]. Broadband noise is generated due to turbulence in the flow interacting with the vanes or the blades. It should be noted that the noise from the high pressure turbine does not effectively radiate out of the engine. Therefore, the turbine noise on the outside of the engine is dominated by the low pressure turbine, which radiates from the aft of engine. The same applies to the compressor, however the noise from the compressor radiates from the inlet of the engine.

2.3. Jet noise

Jet noise is a significant part of the total engine noise, especially during take-off. It was the primary source of engine noise for turbojet engines. The introduction of high bypass ratio engines has reduced jet noise significantly due to the decrease in overall exhaust velocity [24]. But other techniques such as fluid injection or the application of chevrons, depicted in Fig. 2.3, have also been used to reduce jet noise [25]. Jet noise is the result of the jet flow from the engine mixing with the surrounding air [26]. The high speed exhaust intrudes surrounding air (bypass and ambient), which has a relatively lower velocity. This results in turbulence, characterized by broadband noise radiating from the aft of the engine. Particularly, jet noise is known to be highly directional [25]. Additional noise sources occur when the engine is operated outside of its design condition, where the nozzle exit pressure is not equal to the ambient pressures. This leads to the presence of shock cells in the jet exhaust, resulting in broadband shock-associated noise (BBSAN), due to the interaction of the jet shear layer with the shock shells [27]. Broadband shock-associated noise propagates upstream and in the sideline direction relative to the jet flow.

Figure 2.3: Chevrons on GE engine mounted on a Boeing 777 to reduce jet noise [28]

2.4. Fan noise

The fan noise can be separated into four distinct mechanisms [29] as depicted in Fig. 2.4.

1. **Fan boundary layer interaction noise**: This mechanism consists of two interactions. Firstly, the fan blade interacts with the turbulent boundary layer of the inlet duct. The clearance between the tip of the fan blade and the wall of inlet duct is so small that the blade intersects the boundary layer of the wall. This boundary layer is generally turbulent, leading to noise. Secondly, the fan blade interacts with the incoming flow. Generally the incoming flow is distorted due to the shape of inlet, e.g. the drooping and asymmetry. This leads to turbulence in the incoming flow, which in itself produces noise, but also the interaction of this turbulence with the fan produces noise[30].

2. **Fan self-noise**: This is the noise generated by the displacement of the airflow volume. This mechanism is especially relevant at supersonic tip speeds. As shock waves are formed, which can propagate out of the inlet duct [31]. Due to small differences within manufacturing and assembly the tones produced by the blades are harmonic with the rotational speed of the shaft and not with the blade passage frequency (BPF). These tones are so-called buzz-saw noise and radiate from the inlet.

3. **Outlet Guide Vane interaction noise**: This mechanism consists of two interactions. Firstly, the rotating wake of the fan interacts with the outlet guide vanes. This is one of the primary sources of tonal noise [32] and it radiates from the inlet. Moreover, it scales with the blade passage frequency, given by Eq. (2.3). Where B is the number of blades and n_{rot} is the rotational speed of the fan in rotations per minute. Typically, there are also harmonics of this BPF present in the noise spectrum. Secondly, turbulent flow in the fan wake interacts with the outlet guide vanes. This is believed to be one of the major broadband noise sources in fan noise [33].

$$BPF = \frac{Bn_{rot}}{60} \qquad (2.3)$$

4. **Outlet guide vane self noise**: This noise is generated by the scattering of the turbulent flow into acoustic perturbations at the trailing edge of the airfoil or the vane [34]. This principle is known as trailing edge noise and results in broadband noise.
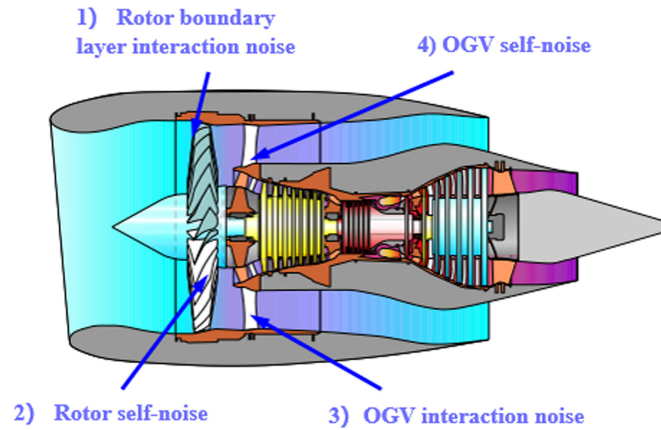

Figure 2.4: The four mechanisms of fan noise

2.5. Directivity

In general the noise coming from the engine is highly directional, due to the nature of the noise generated in the different parts. Figure 2.5 gives good overview of the directivity. The following can be concluded about the directivity of the different parts:

- Fan noise radiates both forward from the inlet and rearward from the exhaust. The noise is characterized by tonal and broadband noise, where the noise from the inlet also contains buzz-saw noise.
- Core noise also radiates both forward from the inlet and rearward from the exhaust. The noise from the inlet is characterized by tonal noise from the low pressure compressor and broadband noise. While the noise from the exhaust is characterized by tonal noise from the low pressure turbine and broadband noise from the combustion. In general core noise is not dominant in the overall spectrum.
- Compressor noise from the inlet is also characterized by tonal noise, however it is not as prominent as the fan noise.
- Jet noise radiates only from the exhaust, unless the engine is outside of its design condition. In that case BBSAN is dominant in the upstream and sideline direction. The jet exhaust is characterized by broadband noise.
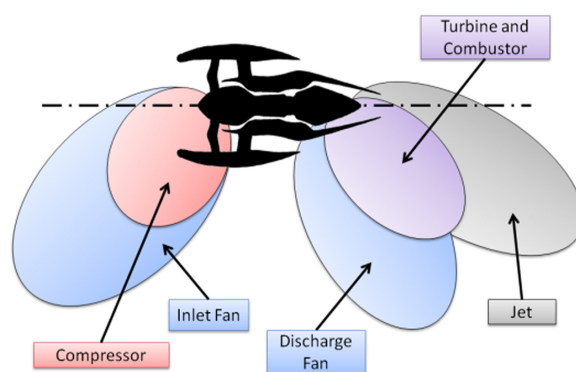
Figure 2.5: Directivity of different noise sources of a turbofan engine [35]

3

Acoustic testing

With a better understanding of the underlying mechanisms of engine noise the focus can be shifted to goals and research questions of this study, which are presented in section 3.1. The experimental setup to acquire the data necessary to answer these research questions is discussed in section 3.2. Moreover, how the data of the experiments is processed is discussed in section 3.3.

3.1. Research questions and goals

As mentioned in chapter 1, the goal of this study is to validate that CLEAN-SC is capable of determining the directivity of static noise sources trough experimentation. Which is a feature that is highly useful for static engine testing. Therefore, the following research question is to be answered:

To what extent is CLEAN-SC capable of determining directivity in the noise breakdown of microphone array data of static engine tests?

The research question is answered by obtaining experimental data with known directivity and then applying the CLEAN-SC tool to this data. So that the results of the ground-truth can be compared to data with multiple sources present. Subsequently from these results it can be determined if the results of Sijtsma on static engine data [4] are precise. Next to the main research question the following sub-questions are to be answered by this study:

- How do the source maps of the experiment obtained by CLEAN-SC compare to other to source maps from conventional frequency domain beamforming and DAMAS?

- What is the effect of the diameter of the pipe on the source maps and the directivity results?

- Is the precision of the directivity breakdown dependent on frequency?

3.2. Experimental setup

The objective of the experiment is to perform reference measurements, for which the location and directivity of the sources can be measured separately so that the ground-truth results can be compared to the outcome of the deconvolution tool CLEAN-SC. The experiments are performed in the anechoic chamber at the faculty of applied sciences at the Delft University of Technology, to minimize background noise levels and sound reflections. The experiment consists of a cylindrical aluminum pipe with two Visaton K 50 SQ speakers [36] inside as reference known sound signals, to simulate a static engine test. The speaker has a baffle diameter of 45 mm, an effective piston area of 12.5 cm^2, and a maximum power of 3 W. Its recommended frequency response range is between 250 Hz and 10 kHz. The speakers are controlled individually so they can be turned on and off separately.

Each speaker faces a different exit of the pipe at a distance of 0.6 m from each opening. Subsequently, the speakers are positioned parallel to the pipe axis, as shown in Fig. 3.3. The sound played by the speakers is white noise so that all frequencies are excited simultaneously. Moreover, both speakers play a different white noise audio file to avoid coherence.

Measurements are repeated for two pipes of different diameters; one with a diameter of 0.45 m (referred to henceforth as big pipe) and the other with a diameter of 0.2 m (referred to as small pipe). Both pipes have the same length of 1.5 m. The choice of aluminium ventilation pipes was made because of their great availability in these formats. The diameters of the pipes have been chosen to analyse the effect of resonance, subsection 3.2.1.

Furthermore, measurements are performed with and without an acoustic-absorbing foam layer in the middle of the pipe. For both pipes, a circular foam layer of the same diameter as the pipe is created by sticking 6 layers of thinner insulation foam on top of each other, achieving a total thickness of 0.1 m. The acoustic-absorbing material used is melamine foam, which is a material commonly used for insulation[1]. The insulation foam circle is placed in the middle of the pipes to prevent leakage of the sound emitted by one speaker positioned on one side of the pipe to the other. This allows the sources to be isolated so that the breakdown of multiple sources can be compared to a single source.

A series of measurements is performed for each pipe with and without foam for comparison purposes. The tests performed for each configuration are listed in Table 3.1. In this example, the tests are performed for the big pipe and no foam inside the pipe. The same measurements are repeated for the big pipe with foam and the small pipe with and without insulation foam. The full test matrix is listed in Appendix A.

Table 3.1: Tests performed per configuration. In this case the pipe configuration is the big pipe, without foam. The values -4 and -10 indicate the decrease in dB of the right speaker volume

meas nr.	left	right	duration (s)
Big Pipe, No foam			
1 background	off	off	10
2	on	off	30
3	off	on	30
4	off	-4	30
5	off	-10	30
6	on	on	30
7	on	-4	30
8	on	-10	30
9 tap test	off	off	10

The acoustic data is recorded for 30 s at a sampling frequency of 50 kHz, using a linear microphone array consisting of 52 PUI Audio POM-2735P-R analog condenser microphones[2]. The microphones have a sensitivity of -35 $\pm$ 2 dB (ref. 1 V/Pa) and a frequency range of 20 Hz to 25 kHz. The microphones are connected to a data acquisition system (DAQ), which is connected to a laptop to record the data. The microphones have an equidistant spacing d of 0.12 m, providing a total length of 6.12 m. As a result, using Eq. (3.1), grating lobes are expected for wavelengths smaller than 0.24 m or frequencies higher than 1.4 kHz. The microphones are taped to thin wooden planks, which are positioned 2.75 m away and parallel to the pipe axis, see Fig. 3.1. Two additional microphones are placed at the exits of the pipe as reference microphones, as shown in Fig. 3.2.

$$d = \frac{1}{2}\lambda \tag{3.1}$$

---

[1] https://www.akoestiekwinkel.nl/flamex-basic-akoestische-platen
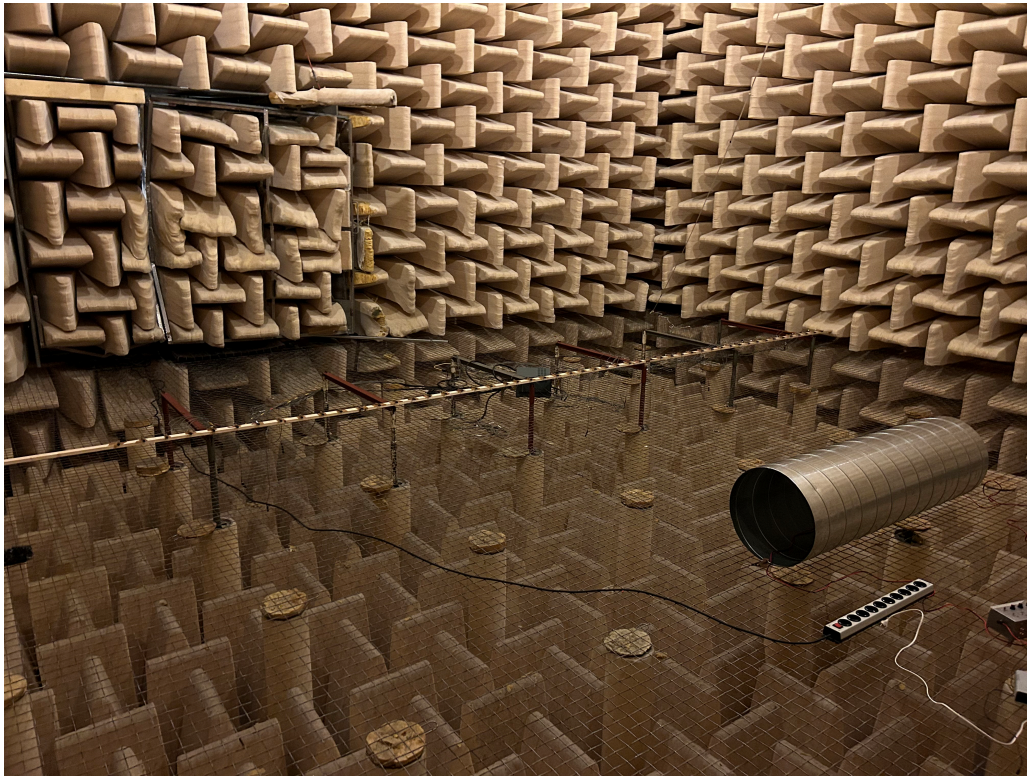[2] https://puiaudio.com/product/microphones/pom-2735p-r

Figure 3.1: Experimental setup with the microphone layout inside of the anechoic chamber.

Figure 3.2: The reference microphone is placed at the exit of the pipe.

Figure 3.3: Speaker and insulation foam placement inside the big pipe. The foam is positioned in the middle of the pipe and the other speaker is positioned in the same manner on the other side of the foam layer.

3.2.1. Resonance

When performing acoustic experiments in a duct, one should be aware of the fact that resonance can occur. A mode will propagate if it is higher than the cut-off frequency and if the mode is lower than the cut-off frequency it will decay exponentially [37]. The cut-off or resonance frequency is given by Equation 3.2.

$$f_c = \frac{j_{m\mu} c_0}{2\pi a} \tag{3.2}$$

Where f_c is the resonance or cut-off frequency in Hz. c_0 is the speed of sound in m/s and a is the radius of the duct. $j'_{m,\mu}$ are the zeros of Bessel functions, with $j'_{1,1}$ = 1.8412 [37] as listed in Table 3.2. Resonance frequencies related to higher order of j also decay or are not as dominant as the lower order frequencies. Therefore the lower order are of greater importance. For the experiment two diameters have been selected such that the for the lower diameter pipe the first resonance frequency falls within the tested spectrum, $f_c = 1005$ Hz for a diameter of 0.2 m. While for the large diameter of 0.45 m $f_c = 447$, which falls outside the tested spectrum.

Table 3.2: Zero's of $j'_{m,\mu}$ from [37]

μ\m	0	1	2	3	4	5
1	0.0000	1.8412	3.0542	4.2012	5.3176	6.4156
2	3.8317	5.3314	6.7061	8.0152	9.2824	10.520
3	7.0156	8.5363	9.9695	11.346	12.682	13.987
4	10.173	11.706	13.170	14.586	15.964	17.313

3.3. Methodology

The data from the experiments is post-processed to obtain acoustic source maps. The source maps are calculated with the following methods: Conventional Frequency Domain Beamforming (CFDBF), DAMAS [38], and CLEAN-SC. Additionally, CLEAN-SC is also used for a directivity breakdown.

For all methods, the acoustic pressure data recorded by each microphone is converted from the time domain to the frequency domain, using a Fourier transform. Moreover, the data is split into snapshots of 5000 samples (0.1 s), where each snapshot overlaps by 50%. Subsequently, Hanning weighting is applied to minimize spectral leakage. Next, for each snapshot, the cross-spectral matrix (CSM, $\mathbf{C}$) is computed by multiplying the pressure amplitudes in the frequency domain by their complex conjugate transpose (indicated by *). The CSM is then obtained by averaging the CSM over all the snapshots:

$$\mathbf{C} = \langle \mathbf{p}_e \mathbf{p}_e^* \rangle \tag{3.3}$$

where e indicates the snapshot number and for each snapshot e and frequency f, $\mathbf{p}_e$ is given by:

$$\mathbf{p}_e(f) = \begin{pmatrix} p_1(f) \\ \vdots \\ p_{N_{mic}}(f) \end{pmatrix}, \tag{3.4}$$

where p_n is the pressure at each microphone for n = 1,..., N_{mic} microphones.

3.3.1. Conventional Frequency Domain Beamforming (CFDBF)

Conventional frequency domain Beamforming (CFDBF) is a frequency domain method and is the most straightforward way to process phased array data [7], as it is fast and robust. The source pressure is modelled at a grid point ξ using the steering vector $\mathbf{g}$ and the source amplitude A. The components g_n model the expected phase variation over the array for a given source position. There are different formulations for the steering vector in the literature depending on the application [39, 40]. For a stationary monopole point source [41] the steering vector can be written as:

$$g_{j,n} = \frac{e^{(-2\pi i f \Delta t_{j,n})}}{4\pi \left\| \mathbf{x}_n - \xi_j \right\|} = \frac{exp\left[\frac{-2\pi i f \left\| \mathbf{x}_n - \xi_j \right\|}{c} \right]}{4\pi \left\| \mathbf{x}_n - \xi_j \right\|}, \tag{3.5}$$

where, c is the speed of sound, $i^2 = -1$, $\mathbf{x}_n = (x_n, y_n, z_n)$, n = 1,..., N_{mic}, $\Delta t_{j,n}$ is the time delay between reception at $\mathbf{x}_n$ and emission at ξ_j, so $||\mathbf{x}_n - \xi_j||$ represents the distance between the source and receiver. The aim is to obtain the source power A at grid point ξ_j by minimizing the difference between the recorded pressure and the modelled pressure:

$$minimize \left(||\mathbf{C} - A\mathbf{g}_j\mathbf{g}_j^*||^2 \right) \tag{3.6}$$

Solving for the source power gives:

$$A(\xi) = \frac{\mathbf{g}_j^* \mathbf{C} \mathbf{g}_j}{||\mathbf{g}_j||^4} \tag{3.7}$$

This expression is known as "Conventional Beamforming". Now Eq. (3.7) can be shortened by the introduction of the weighted steering vector at scan point ξ_j:

$$\mathbf{w_j} = \frac{\mathbf{g}_j}{\mathbf{g}_j^* \mathbf{g}_j} = \frac{\mathbf{g}_j}{||\mathbf{g}_j||^2}, \tag{3.8}$$

in that case Eq. (3.7) becomes Eq. (3.9):

$$A_j = \mathbf{w}_j^* \mathbf{C} \mathbf{w}_j \tag{3.9}$$

3.3.2. DAMAS

The Deconvolution Approach for the Mapping of Acoustic Sources (DAMAS) is a tool developed by Brooks and Humphreys to improve upon the CFDBF results by accounting for the presence of multiple sources. The tool solves the following inverse problem so that the source strength distributions are extracted from the CFDBF acoustic source maps [38]:

$$\mathbf{y} = \mathbf{A}\mathbf{x}. \tag{3.10}$$

The number of grid points is given by J, thus $\mathbf{y} \in \mathbb{R}^{J \times 1}$ with $\mathbf{y}$ representing the source power output obtained from the conventional beamforming, $\mathbf{x} \in \mathbb{R}^{J \times 1}$ is the so-called equivalent source distribution at the same grid locations. Because of finite resolution and sidelobes $\mathbf{x} \neq \mathbf{y}$. $\mathbf{A} \in \mathbb{R}^{J \times J}$ is the propagation matrix. Each column of $\mathbf{A}$ contains the point spread function (PSF) of that corresponding grid point j. Equation 3.10 is generally solved using a Gauss-Seidel iterative method [3], with the constraint that the source powers $\mathbf{x}$ are positive. This typically requires thousands of iterations to obtain a source map, which can become an issue for large $\mathbf{A}$ as the computation time scales scales with J^3. However, in the current study, computational time should not pose a problem, because a one-dimensional scan grid is used, which significantly reduces the amount of grid points required to provide the desired accuracy.

3.3.3. CLEAN-SC

CLEAN-SC is a frequency-domain deconvolution method developed by Sijtsma [7]. The method makes use of the fact that the main lobes are spatially coherent with their sidelobes. These sidelobes are removed from the CFDBF source maps in an iterative manner, to obtain a clean map. The CLEAN-SC method works in the following way.

For one frequency or a frequency band, a peak source is searched in the *dirty map* obtained from CFDBF. This peak source is then removed from the CSM and replaced by a clean beam (beam without sidelobes) in the *clean* source map. Afterwards, the degraded CSM is used to compute an updated dirty map, in which the first peak source has been removed. A new peak source is searched in the updated dirty map and again removed from the degraded CSM and a clean beam is added to the *clean* source map. This process is repeated until a stop criterion is reached. This criterion can be a maximum number of iterations or when the *clean* CSM contains significantly more information than the degraded CSM.

The process at each iteration can be written in terms of the following steps. The maximum value in the dirty map at scan point $\vec{\xi}_j$ is searched, which is equal to CSM multiplied by a set of weighted steering vectors $\mathbf{w}_j$:

$$max(A_j) = A(\vec{\xi}_j) = \mathbf{w}_j^* \mathbf{C} \mathbf{w}_j. \tag{3.11}$$

In this case, there is no distance correction in the steering vector, thus Eq. 3.8 becomes:

$$\mathbf{w}_j = \frac{\mathbf{g}_j}{N_{mic}} \tag{3.12}$$

The contribution of a sound source to the CSM can be expressed in terms of the *source component* $\mathbf{h}_j$, noted as Eq. (3.13). $\mathbf{h}_j$ can be seen as an improved version of steering vector $\mathbf{g}_j$, as it better represents the unknown source vector $\mathbf{p}_j$.

$$\mathbf{h}_j = \frac{1}{(A_j)_{max}}\mathbf{C}\mathbf{w}_j = \frac{\sum_{k=1}^{K}\mathbf{p}_k(\mathbf{p}_k^*\mathbf{w}_j)}{(A_j)_{max}}, \tag{3.13}$$

where K is the number of sources and $\mathbf{p_k}$ is the source vector from the kth source. Using this definition of the source component $\mathbf{h}_j$, $\mathbf{p}_j\mathbf{p}_j^*$ can be estimated by Eq. (3.14):

$$\mathbf{p}_j\mathbf{p}_j^* = (A_j)_{max}\mathbf{h}_j\mathbf{h}_j^*. \tag{3.14}$$

This estimate is then multiplied with the loop gain ϕ, $0 < \phi \leq 1$ as a safety factor [7] and subtracted from the CSM. For this paper the loop gain is varied depending on the experimental data, but for most cases a loop gain of 0.1 is selected. So that the new degraded CSM for the next l^{th} iteration can be written as:

$$C^{(l)} = C^{(l-1)} - \phi A_{(j),max}\mathbf{h}_j\mathbf{h}_j^*. \tag{3.15}$$

After L iterations, the original complete CSM can be written as the summations of the source components plus the degraded CSM, which is denoted as $\mathbf{D}$, Eq. (3.16). If a sufficient number of iterations is performed $||\mathbf{D}^{(L)}|| << ||\mathbf{C}^{(L)}||$. This indicates that the clean CSM contains significantly more information than the degraded CSM. In that case, the complete CSM can be approximated by the first term on the right-hand side of Eq. (3.16):

$$\mathbf{C}^{(L)} = \phi \sum_{j=1}^{L}(A_j)_{max}\mathbf{h}_j\mathbf{h}_j^* + \mathbf{D}^{(L)} \approx \phi \sum_{j=1}^{L}(A_j)_{max}\mathbf{h}_j\mathbf{h}_j^*. \tag{3.16}$$

3.3.4. Directivity breakdown

In addition to creating the source map of the array data, CLEAN-SC can also be used to perform source power integration and directivity analysis. For each iteration *l* a maximum source was localized at the associated scan point ξ_j, hence the location of the source in the map is known. Moreover, if the source is static (so it is not moving in time), it is possible to assign sound sources to specified areas or parts. As a result, the CSM can be written as the sum of different sources from predefined areas, which is especially applicable to static engine noise testing. In essence the CSM can be split into separate CSM's containing the contributions of certain components. In that case, Eq. (3.16) can, for example, for each iteration *l* be written as breakdown of engine noise sources (e.g. intake, bypass, core, and jet) as done by Sijtsma [4]:

$$\mathbf{C} = \left(\sum_l A_l\mathbf{h}_l\mathbf{h}_l^*\right)_{intake} + \left(\sum_l A_l\mathbf{h}_l\mathbf{h}_l^*\right)_{bypass} + \left(\sum_l A_l\mathbf{h}_l\mathbf{h}_l^*\right)_{core} + \left(\sum_l A_l\mathbf{h}_l\mathbf{h}_l^*\right)_{jet}. \tag{3.17}$$

In the same way for iteration *l* of CLEAN-SC, the sources in the current experiment can be split into contributions from left, right, and other:

$$\mathbf{C} = \left(\sum_l A_l\mathbf{h}_l\mathbf{h}_l^*\right)_{left} + \left(\sum_l A_l\mathbf{h}_l\mathbf{h}_l^*\right)_{right} + \left(\sum_l A_l\mathbf{h}_l\mathbf{h}_l^*\right)_{other} \tag{3.18}$$

Not only can sources be localized, but it is also possible to extract information about their directivity, by considering the individual diagonal elements of the split CSM. This way, CLEAN-SC is capable of providing directivity information of separate source areas.

In order to provide a noise breakdown, the source areas have to be defined. For the DGEN380 static engine tests, the areas are dependent on individual noise sources of the engine, as displayed in Fig. 3.4a. In this case, the sources are not symmetric and therefore neither are the selected areas. However, in the case of the current experimental setup, the sources are symmetric, hence, it makes sense to define the areas symmetrically as displayed in Fig. 3.4b. The source areas are set at ± 0.15 m in each direction of the pipe exits.
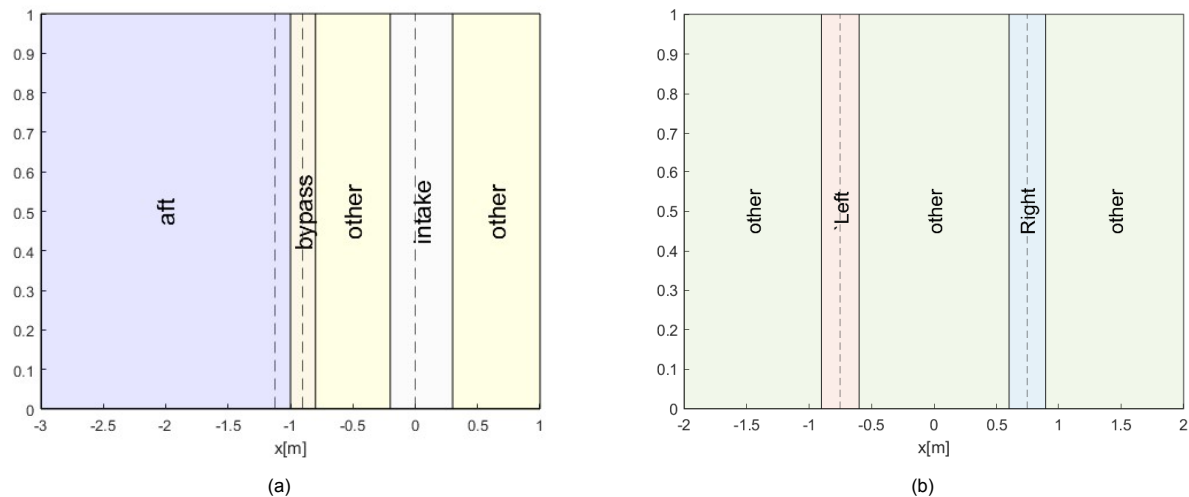
Figure 3.4: The noise source areas, the dotted lines in (a) indicate from left to right; core exhaust, bypass exhaust, and intake [4], while in (b) they indicate; left pipe outlet and right pipe outlet.

4

Results & Discussion

In this chapter the results of the experiments are presented and analysed. First in section 4.1, the microphone spectra are analysed to asses the performance of the speakers, the insulation foam and the microphones in the array. In addition the tap tests are also analysed. Secondly, in section 4.2 the acoustic source maps of the experiment are presented. Thirdly, in section 4.3 the directivity breakdown of the experimental data is shown and its precision is analysed. Finally a more detailed analysis of the precision of the directivity breakdowns is performed in section 4.4.

4.1. Analysis of the microphone spectra

This section focuses on microphone spectra. The spectra of the reference microphones are analysed to confirm the effect of the insulation foam and to compare the speaker performance in subsection 4.1.1. To analyse the performance of the array, the spectrum of each microphone in the array is compared in subsection 4.1.2. Finally, the tap tests are also analysed by looking spectra of the reference microphones in subsection 4.1.3.

4.1.1. Reference Microphones & Speaker Performance

As discussed in chapter 3, two microphones are placed at the exits of the pipe. These are used as reference microphones. The averaged spectra of these microphones can be used to compare the performance of the speakers and also to asses the performance of the insulation foam. The spectra of the reference microphones is shown in Fig. 4.1. The effect of the foam is visible in both Fig. 4.1a and Fig. 4.1b. When analysing the figures it can be seen that for both sides, the overall level of the recorded noise is significantly decreased due to the addition of the insulation foam. It is also noticeable that insulation foam performs better for higher frequencies.
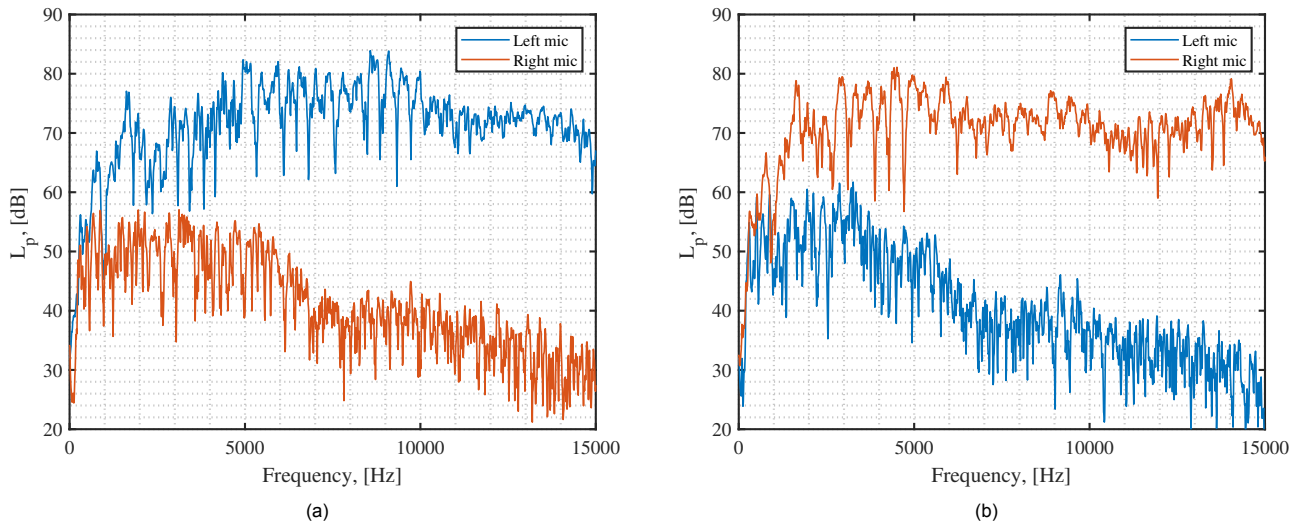
Figure 4.1: Spectra of the reference microphones for the big pipe with foam (a) for the left speaker "on" and (b) for the right speaker "on".

Furthermore, the reference microphone spectra can also be used to compare the speakers. This is done by analysing the microphone spectra of tests with foam and both speakers "on". The foam effectively blocks leakage of noise to the other side of the pipe, hence the speakers are isolated. In Fig. 4.2 the spectra of the reference microphones are shown for the cases when both speakers are turned "on" and foam is present inside the pipes. In both plots it is visible that the speaker performance below 500 Hz is limited, which is expected as the speakers are relatively small. Therefore, further analysis will focus on frequencies above 500 Hz. In addition, it also appears that right speaker produces slightly higher noise levels for frequencies below 5000 Hz and above 5000 Hz the left speaker produces slightly more noise. Moreover, the frequency range is limited to 10 kHz as this is the top of the recommended frequency response range of the speakers. When comparing the big and the small pipe, it can be observed that the amplitude peaks in the spectrum of the small pipe are a bit higher than for the big pipe, which can be attributed to the fact that the small pipe has a smaller diameter. As a result the sound is spread over a smaller area which leads to higher peaks and a slightly higher noise amplitude overall for the same speaker setting.
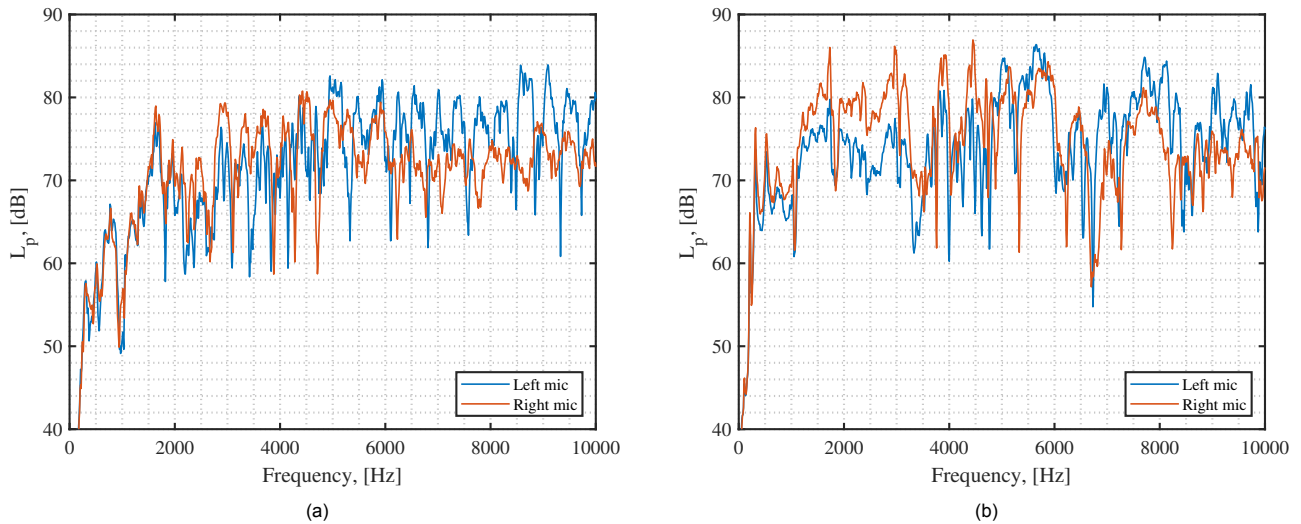

Figure 4.2: Average spectra of the reference microphones for both speakers "on" (a) for the big pipe and (b) for the the small pipe.

4.1.2. Microphone Array Performance

In addition to checking the speaker performance, also the performance of the microphones in the array can be checked. In Fig. 4.3 the average spectra of all microphones in the array per 1/3 octave band is shown for the big pipe in Fig. 4.3a and for the small pipe in Fig. 4.3b. The spectra are shown per 1/3 octave band to allow for more simple differentiation between the individual microphone spectra. In both plots the average spectrum of all microphones is represented by the black line. In both plots it can be observed that some microphones record sound levels higher than the average and others record levels lower than the average. Part of this deviation is expected, due to the fact that some microphones are closer to the source than others. The difference between the microphone closest and the one furthest away is around 2.5 dB, using Eq. (4.1), where R_1 is the distance to furthest source, R_2 distance to the closest source and ΔSPL is the difference in dB. However, in both plots the spread from the average spectrum increases at frequencies above 5000 Hz. This indicates that some microphones start to display an amplitude off-sets at higher frequencies, since their position has not changed. This is important to take note of especially for the directivity breakdown, as individual microphone data is considered in the breakdown and amplitude off-sets have an effect on the analysis.

$$\Delta SPL = 20 \log\left(\frac{R_1}{R_2}\right) \tag{4.1}$$
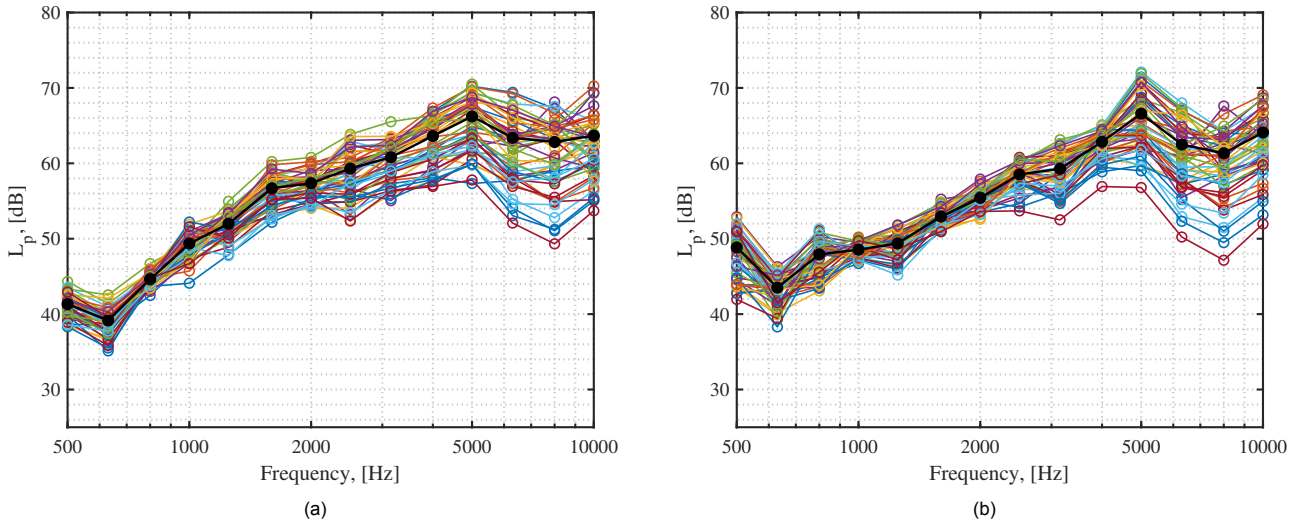

Figure 4.3: Spectra of the all microphones in the array for 1/3 octave bands. The black line indicates the average spectrum of all microphones in the array (a) for the big pipe and (b) for the small pipe with both speakers "on" and no foam

4.1.3. Tap Tests Results

The best way to asses the data from the tap tests is to analyse the spectra of the reference microphones of these tests, which are shown In Fig. 4.4. The black dotted lines in the plots indicate the locations of the first, second and third resonance frequency of the pipes. It can be observed that for both the big and the small pipe, there appears to be no frequency peak at these resonance frequencies. Moreover, there are also no peaks visible in the plots in Fig. 4.2. Therefore, it can be concluded that these resonance modes do not have a significant effect on the noise spectra of the tests. However, there is another form of resonance visible in the plots. For the big pipe in Fig. 4.4a, there is resonance up to 4000 Hz and for the small pipe in Fig. 4.4b up to 2500 Hz. This is most likely, the response of the structure of the pipe to the tap. So it can be classified as structural resonance.
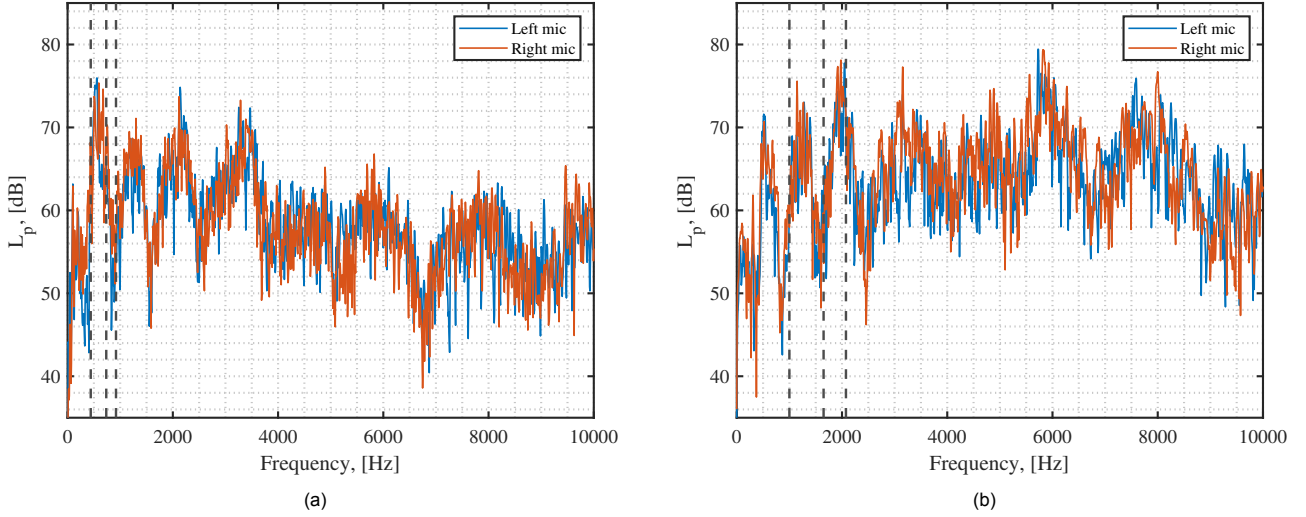
Figure 4.4: Spectra of reference microphones for the tap tests (a) for the big pipe with no foam and (b) for the small pipe with no foam

4.2. **Acoustic Source Maps**

With the methods described in chapter 3 the array data from the experiments is processed to obtain source maps and the directivity breakdown. In this section the source maps obtained from Conventional Frequency Domain Beamforming (subsection 4.2.1), DAMAS (subsection 4.2.2) and CLEAN-SC (subsection 4.2.3) are presented and the results are discussed.

4.2.1. **Conventional Frequency Domain Beamforming (CFDBF)**

The first analysis of the data is performed by making source maps using conventional frequency domain beamforming, as this is a quick and standard method to analyse microphone array data. The source maps are made with a scan grid ranging from -3 m to 3 m with a step size of 0.01.

In Fig. 4.5 beamforming plots of two cases are shown. The case in Fig. 4.5a is the big pipe with the left speaker on and no foam while the same case with insulation foam inserted in the pipe is shown in Fig. 4.5b. The exits of the pipe are indicated by the black dotted lines in the figure. The exits are located at x = -0.75 and x = 0.75, respectively. The location of the exits is the same for all tests, including the small and the big pipe. The effect of the foam is observable by comparing the source maps. In Fig. 4.5a the left speaker is on, but since there is no foam, leakage occurs. This is visible in the plot due the presence of sources at the right exit of the pipe. This leakage is not present after the insertion of the foam as can be seen in Fig. 4.5b. This indicates that the insulation foam reduces the leakage significantly, which is its intended purpose.
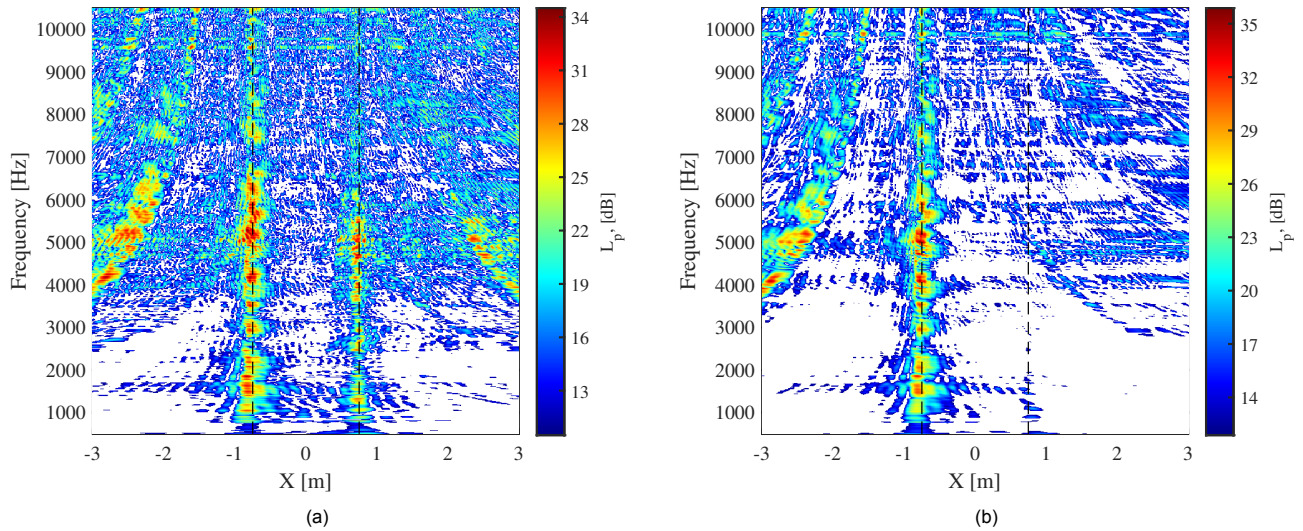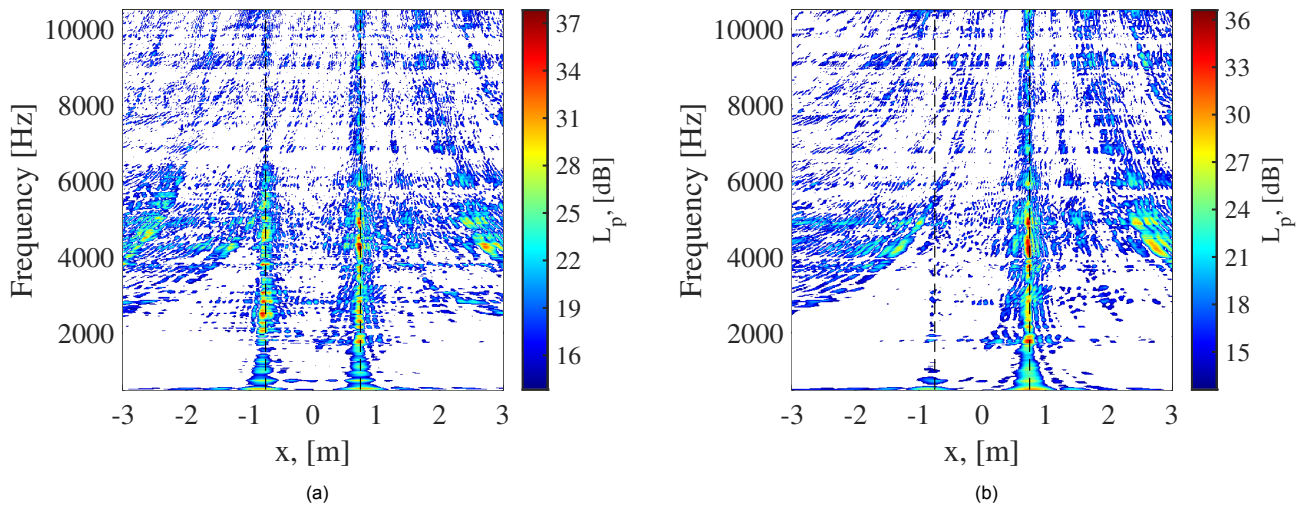
Figure 4.5: CFDBF acoustic source maps for the big pipe with the left speaker "on" without (a) foam and (b) with foam (b). The black dotted lines indicate the exits of the pipe.

In Fig. 4.6 the effect of the foam in the small pipe is shown. In Fig. 4.6a only the right speaker is on and no insulation foam is inserted into the pipe. Again, leakage to the left side of the pipe is visible in the plot. In Fig.4.6b this leakage is not present, indicating that also in the small pipe the insulation foam is functioning as desired. When comparing the source maps for the big and the small pipe, it is observable that for the big pipe the sources are more scattered around the exit compared to the small pipe, where the sources are located more in line with the pipe exit. This can be explained by the fact that a wider opening will lead to more scattering of the sound compared to a smaller opening.

Figure 4.6: CFDBF acoustic source maps for the small pipe with the right speaker "on" and (a) no foam and (b) with foam. The black dotted lines indicate the exits of the pipe.

The plots also indicate the fact that the foam is required in order to be able to distinguish between leakage and actual noise for CFDBF. In Fig. 4.7 a case with and without foam is shown. For both cases the left speaker is on full volume, while the right speaker is set 10 dB lower. It can be seen that for the case without foam leakage from the left speaker is overshadowing the sound produced by the right speaker. This can be observed by comparing the beams at the right exit in Fig. 4.7a to the beams in Fig. 4.7b. The right speaker is on, but it is not distinguishable from the leakage, which highlights the effect of the insulation foam.
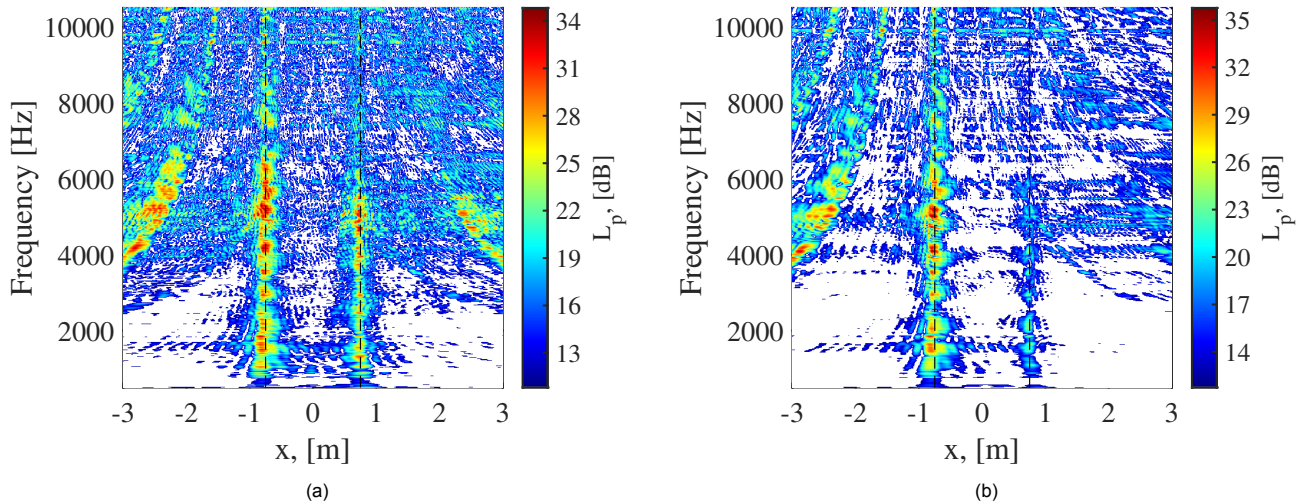
Figure 4.7: CFDBF acoustic source maps for big pipe with the left speaker "on" and the right speaker at -10 dB lower than the left in (a) no foam and (b) with foam. The black dotted lines indicate the exits of the pipe.

Another aspect that is noticeable in the source maps is that there are large grating lobes visible in all plots. Especially for the big pipe grating lobes are visible on the side for which the speaker is turned on. In between the 4000 Hz and 6000 Hz and x=-3 m and x=-2 m the grating lobes are similar in amplitude to the real source, which is undesirable. The benefit of this experiment is that the location of the sound sources are known, however in real world engine testing this is not the case, hence a better method to distinguish sources and grating lobes is desired.

4.2.2. DAMAS

A method that should provide a better quality source map is DAMAS. As discussed in subsection 3.3.2, DAMAS uses an inverse method to obtain a better source map. As a result it is computationally expensive, as it scales with J^3. The scan grid used in the experiment is only 1D, which make DAMAS a computationally viable option for making clear source maps, without excessive computation time. The source maps are made using 300 iterations of DAMAS, with a scan grid ranging from -3 m to 3 m and a step size of 0.03.

In Fig. 4.8 the same cases as in Fig. 4.5 are shown. In Fig. 4.8a the case of the big pipe with no foam and the left speaker on is displayed, while in Fig. 4.8b the same case with foam is shown. Again the effect of the insulation foam is clearly visible. In addition the plots do not contain as much distortion as the CFDBF plots, but there are still grating lobes visible in the plot. But in general the quality of the source map is improved.
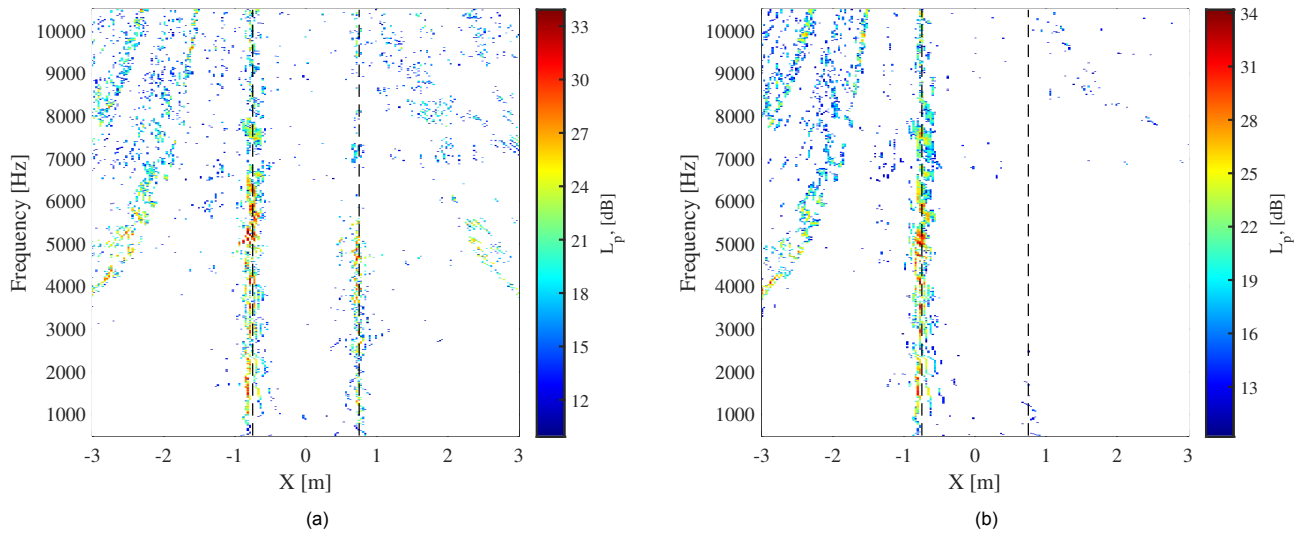
Figure 4.8: DAMAS acoustic sources maps for big pipe with the left speaker "on" and no foam (a) and with foam (b). The black dotted lines indicate the exits of the pipe.

Furthermore, when comparing the source maps of the big pipe Fig. 4.9a and the small pipe Fig. 4.9b, the sources for the small pipe lie more in line with the exit compared to the big pipe. This can be seen in Fig. 4.9, the sources are more scattered around exit the for the big pipe than for the small pipe. This is also visible in the plots from CFDBF, but it becomes more clear in the plots from DAMAS. A simple for reason for this, is that the big pipe has a larger diameter, which allows to sound to spread more, compared to the small pipe, where the sound is more concentrated. Which is also why the maximum noise level in the results of the small pipe is a little bit higher.
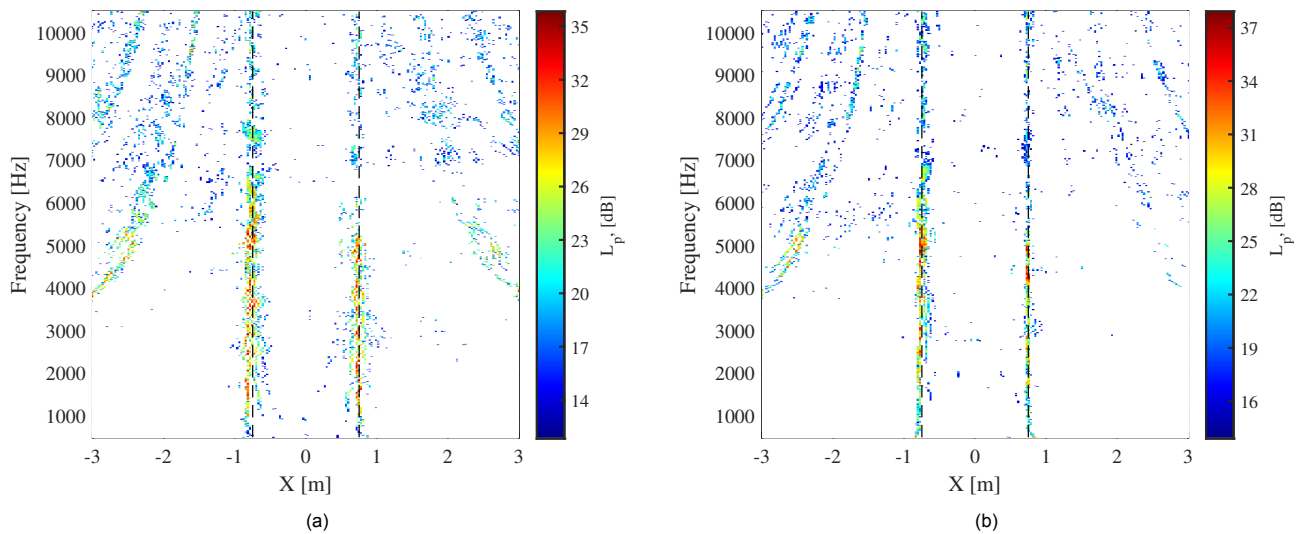

Figure 4.9: DAMAS acoustic source maps no foam and both speakers "on" for (a) the big pipe and (b) the small pipe

4.2.3. CLEAN-SC

The main part of the analysis is performed by applying the CLEAN-SC method to the data. The settings to obtain the source maps are varied depending on the case that is analysed. For all cases the scan grid ranges from -3 to 3 with a step size of 0.01. Moreover, a stop criterion is formulated. The iterations stop when the norm of the degraded CSM is smaller than 0.3 of the original CSM or the maximum number of iterations of 350 is reached. These settings provided good results for most cases, however in some cases such as the cases with one speaker on and the other speaker at low volume the criteria are tweaked to obtain better results. As in

these instances the algorithm favors the side with the high volume speaker, hence in order to not lose the information of the lower speaker the stop criterion is decreased and the maximal number of iterations is increased, subsequently the loop gain is also decreased for these cases.

In Fig. 4.10, the results of CLEAN-SC are displayed, for the case of the big pipe with the left speaker on with foam and without foam. It can be observed that the source map is more clear compared to conventional frequency domain beamforming and DAMAS. In addition it is noticeable that there are almost no grating lobes present. Nonetheless above 7000 Hz, some grating lobes start appear. Moreover when comparing the source maps in the case without foam has slightly more grating lobes than the case with foam. This trend is also visible for the small pipe in Fig. 4.11, when comparing Fig. 4.11a and Fig. 4.11b. What is also noticeable when comparing the acoustic source maps of the big pipe to small pipe, is that the beams are more scattered around the exits compared to the small pipe, which is also noted for the DAMAS and CFDBF source maps.

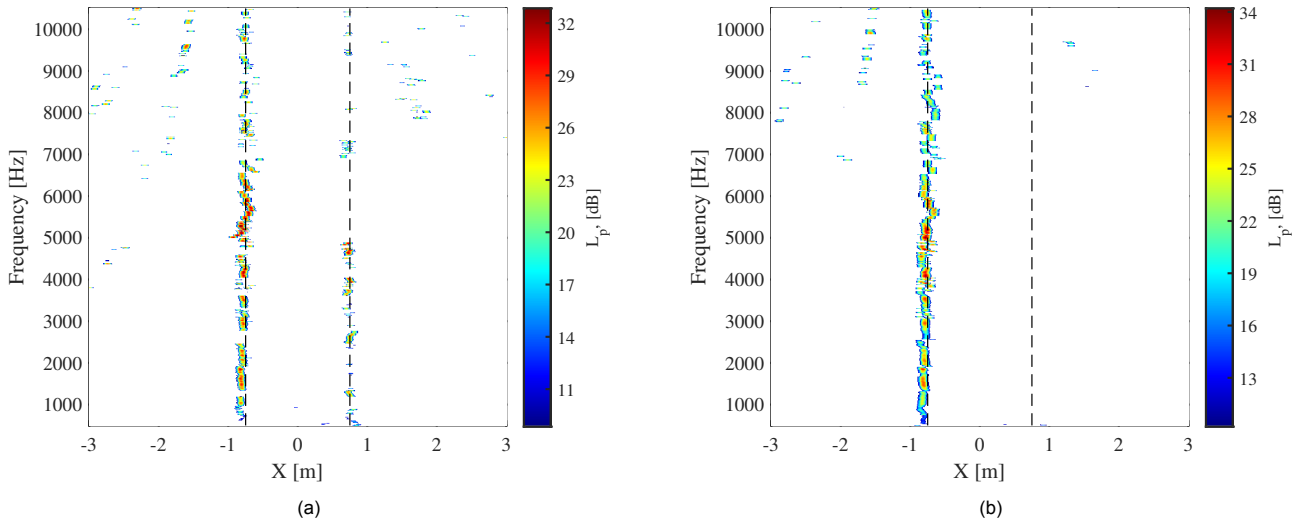(a)   (b)

Figure 4.10: CLEAN-SC acoustic source maps for the big pipe and the left speaker "on" (a) without foam and (b) with foam. The black dotted lines indicate the exits of the pipe.
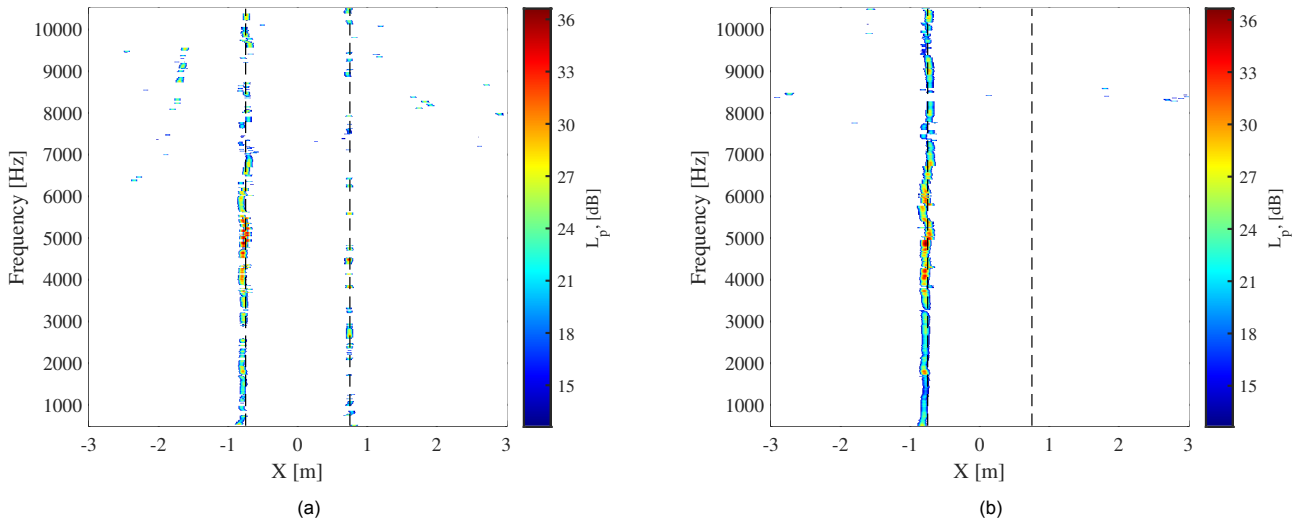

(a)   (b)

Figure 4.11: CLEAN-SC acoustic source maps for the small pipe and the left speaker "on" (a) without foam and (b) with foam. The black dotted lines indicate the exits of the pipe.

The acoustic source maps from CLEAN-SC for the big pipe and the small pipe with no foam and the right

speaker turned on are shown in Fig 4.12 and Fig. 4.13, respectively. In the source maps, the leakage to other exit of pipe is clearly visible. Now, what is interesting to note is that because CLEAN-SC relies on spatial coherence it can only put a source on the left or the right exit for a certain frequency, as there is only one source. If the leakage is sufficient, CLEAN-SC selects to put a source on the opposite side of the turned on speaker. This effect is clearly visible in both Fig. 4.12a and Fig. 4.6a at around 3000 Hz. Here CLEAN-SC has located a number of sources at the left exit and as a consequence it can not display sources at the right exit, due to coherence.

Would this have any implications for static engine tests? In general the noises sources in a turbofan engine are not coherent as they are mainly broadband. So when leakage occurs, CLEAN-SC will most likely treat it as a new source, in addition to the main source. Which could lead to a different issue. Namely that the source can contribute to a different source area, depending on how the source areas have been defined. For example, when broadband compressor noise leaks trough back of the engine, CLEAN-SC would register a new source. However, since it is at the back of the engine the source would most likely lie in the area of the core or the exhaust. So its contribution in the breakdown will fall under these areas, even though it originated from the compressor. Now it is unlikely that noise from the compressor will leak to the back of the engine or that it has a large contribution to the total noise of the core or the jet. So it is most likely not an issue for the overall breakdown. However, it also highlights why it is difficult to separate the core and the jet noise, as they are very close in proximity. With regards to the coherence issue, the only place where this can occur is through leakage of fan tones through the bypass. Sijtsma solves this issue by removing shaft order tones from the microphone signal [4].
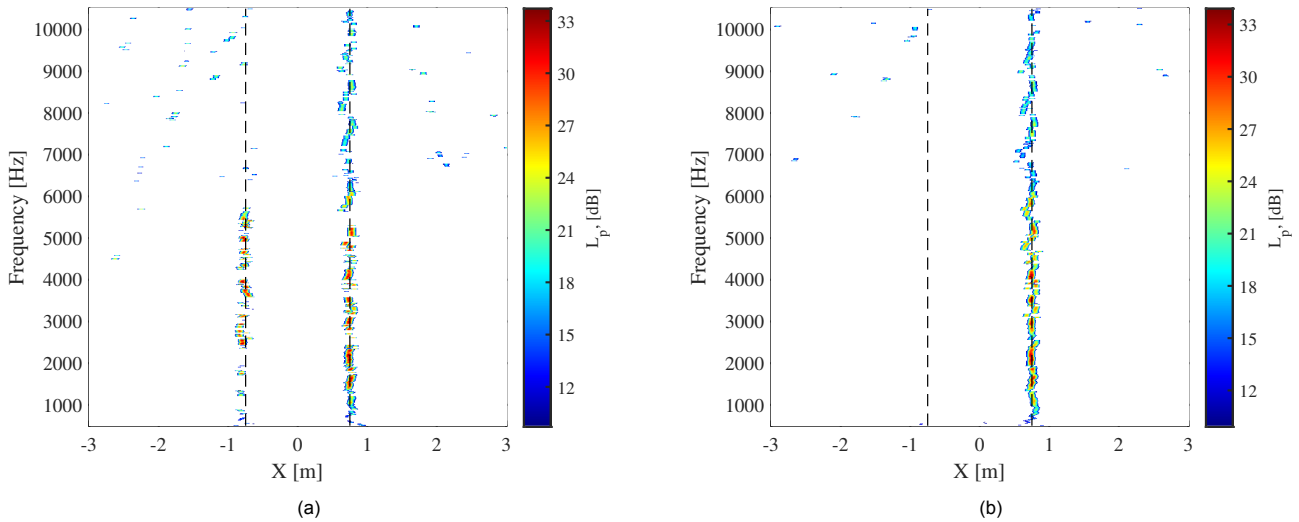

Figure 4.12: CLEAN-SC acoustic source maps for the big pipe with the right speaker "on" and (a) no foam and (b) with foam
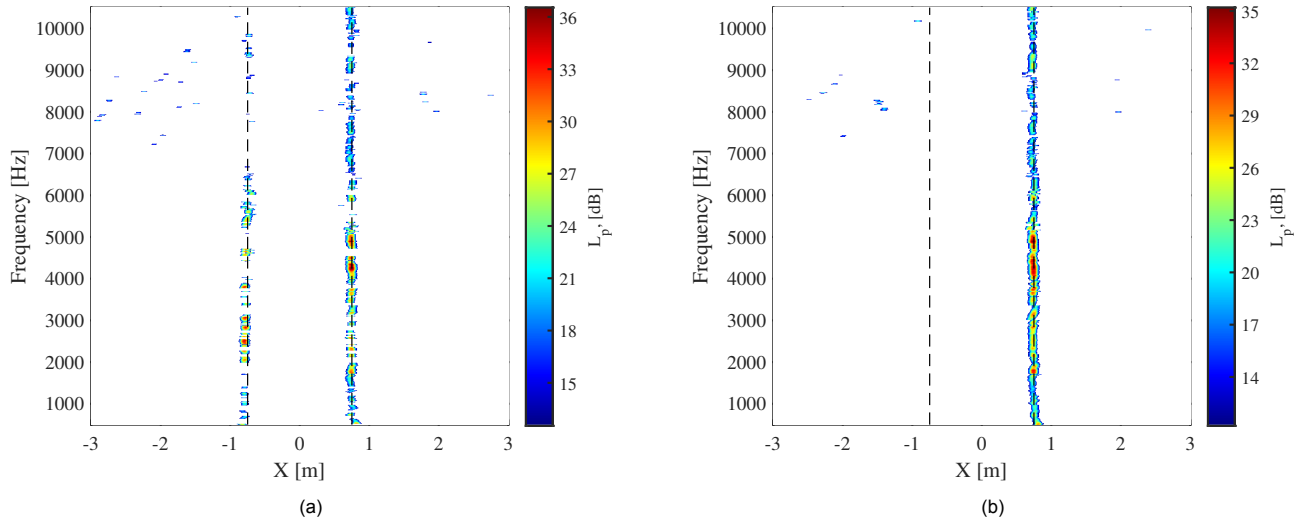
Figure 4.13: CLEAN-SC acoustic source maps for the small pipe with the right speaker "on" and (a) no foam and (b) with foam

Acoustic source maps are also made for the big pipe with both speakers on with and without foam, which are shown in Fig. 4.14. In addition the acoustic source maps for the small pipe with both speakers on with and without foam are depicted in Fig. 4.15. Again, it is observable that grating lobes start to appear above 7000 Hz. Moreover, almost all sources are in line with the exits of the pipe. However, the sources at the left exit display a small off-set with respect to the exit of the pipe when compared to the right side. This off-set is tiny, so it should not have an effect on the breakdown, as long as the sources fall in the correct area. When comparing the acoustic source maps of the big pipe to the small pipe, the same effects as previously mentioned are noticeable; namely, that there is more scattering of sources for the big pipe compared to small pipe. Additionally, there are also more grating lobes visible in the plots for the big pipe compared to the small pipe.
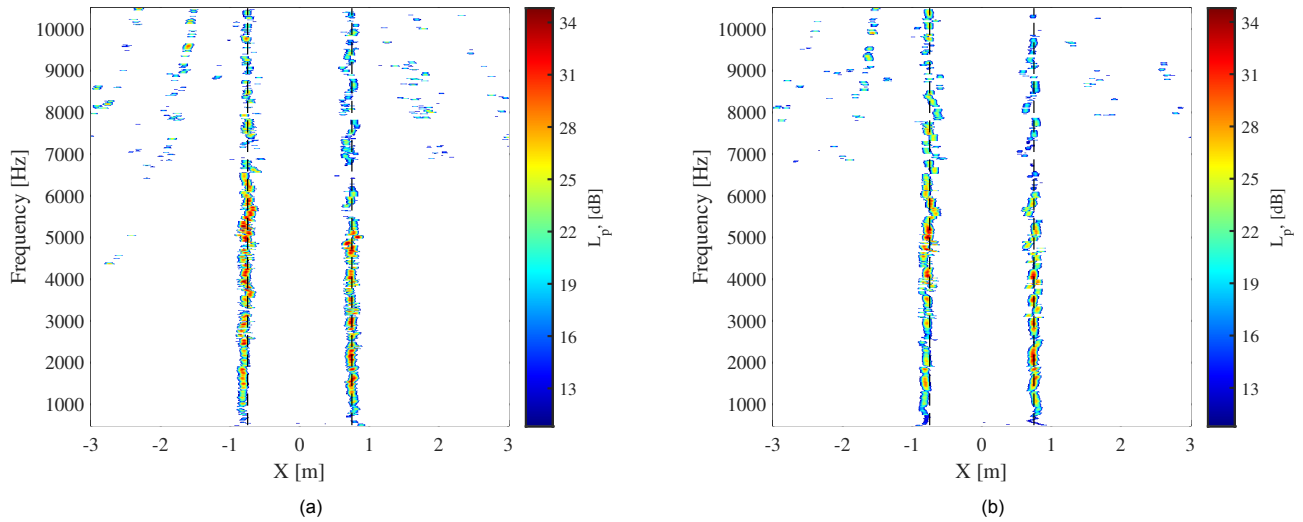

Figure 4.14: CLEAN-SC acoustic source maps for the big pipe with both speakers "on" and (a) no foam and (b) with foam
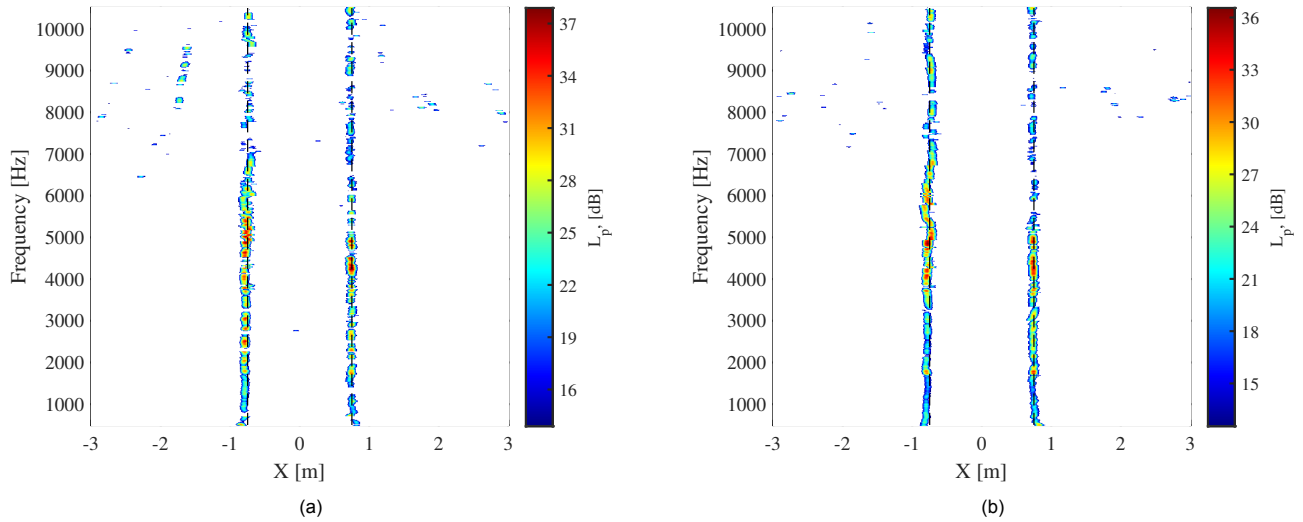
Figure 4.15: CLEAN-SC acoustic source maps for the small pipe with both speakers "on" and (a) no foam and (b) with foam.

The final acoustic source maps of interest originate from the tests with left speaker on full volume and the right speaker speaker at a volume of 10 dB lower than the right speaker. In Fig. 4.16, the acoustic source maps for the big pipe with and without foam are shown and similarly for the small pipe in Fig 4.17. The settings of CLEAN-SC to obtain these results are tweaked compared to other maps, as more iterations and a smaller loop gain are required to detect the sources on the right side. The loop gain is set at 0.05 and the maximum number of iterations is increased to 1700. Subsequently, the stopping criterion is also lowered so that the iterations stop when the norm of the degraded CSM is smaller than 0.2 of the original CSM or the maximum number of iterations is reached. By comparing the cases without foam Fig. 4.16a and Fig. 4.17a and the cases with foam with foam in Fig 4.16b and Fig. 4.17b, it can be observed that the sources at the right exit with no foam have an higher amplitude than the sources at the right exit for the cases without foam. This can be attributed to leakage of sound to the other exit of the pipe. Since the sources originating from the right speaker are weak compared to the sources on the left side, they are overshadowed, but as a consequence the source can not be located at the right exit anymore due to coherence. This effect can be observed in Fig. 4.16a around 4800 Hz, where there are strong sources at the right exit and as a result these are not present at the left exit. In general CLEAN-SC is able to detect the sources at the right exit for the cases with foam, even when the right speaker is at a lower volume compared to the left.
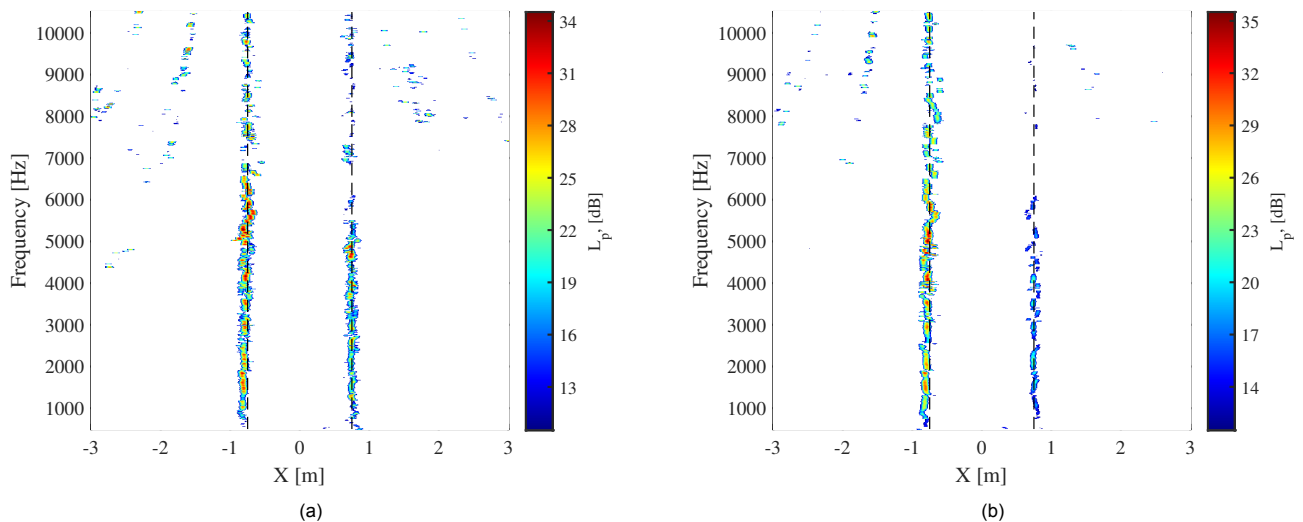

Figure 4.16: CLEAN-SC acoustic source maps for the big pipe with the left speaker on full volume and the right speaker at 10 dB lower and (a) no foam and (b) with foam
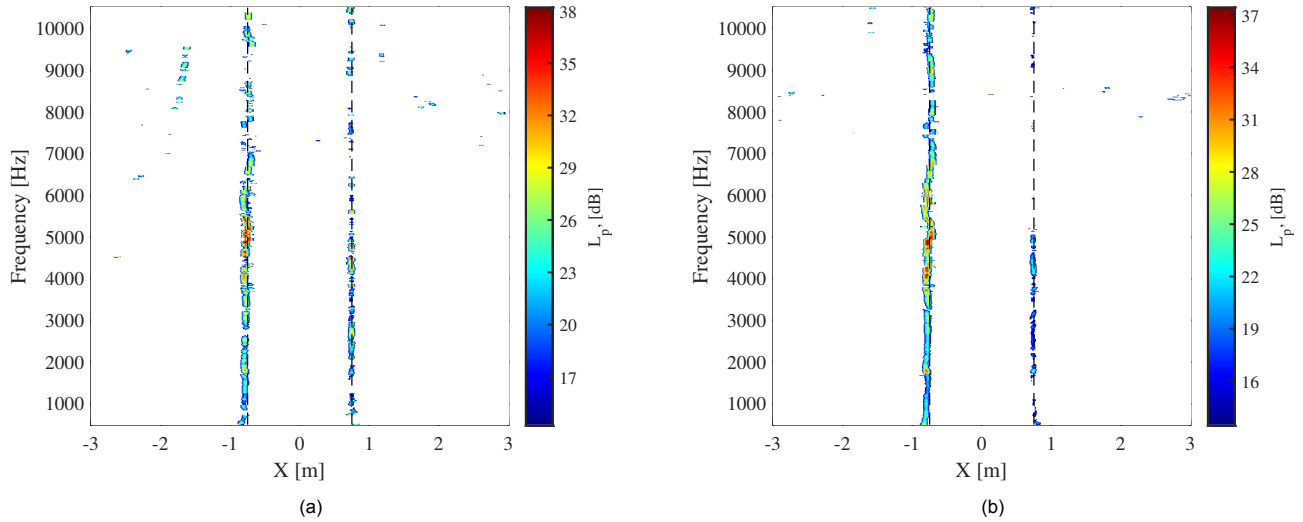
Figure 4.17: CLEAN-SC acoustic source maps for the small pipe with the left speaker on full volume and the right speaker at 10 dB lower and (a) no foam and (b) with foam

4.3. Directivity breakdown

The overall goal of the study is to see if CLEAN-SC is capable of a precise directivity breakdown. This section will investigate this capability of CLEAN-SC. Moreover, this section focuses on results of the big pipe, because the breakdown results of the small and the big pipe are very similar. In addition, all cases discussed include foam insulation, as this allows for isolation of the speakers, which is required for accurate breakdown. Otherwise, the directivity breakdown is affected by leakage.

The acoustic source maps from CLEAN-SC are also used to perform the directivity breakdown. As explained in section 3.3, the CSM is decomposed into contributions from separate source areas. By considering the diagonal elements, information about the directivity is extracted and a noise source breakdown can be performed. The source areas employed are defined as depicted in Fig. 3.4b, where both the left and the right area cover ± 0.15 *m* from each of the exits of the pipe, providing a total width of 0.3 m. The rest of the sources fall into the category *other*. The directivity breakdown is performed for one-third-octave bands centered around a selected frequency. For instance, in Fig. 4.18, the directivity breakdowns for a one-third-octave band centered at 3150 Hz are depicted for the left speaker on and the right speaker on. In these figures, the lines correspond to the respective contributions of the areas in Fig. 3.4b. Subsequently, the category *all* corresponds to the total sum of the noise levels from all areas. The overall analysis is limited to 5000 Hz due to the fact that at higher frequencies the microphones suffer slight amplitude off-sets, as seen in Fig. 4.3.
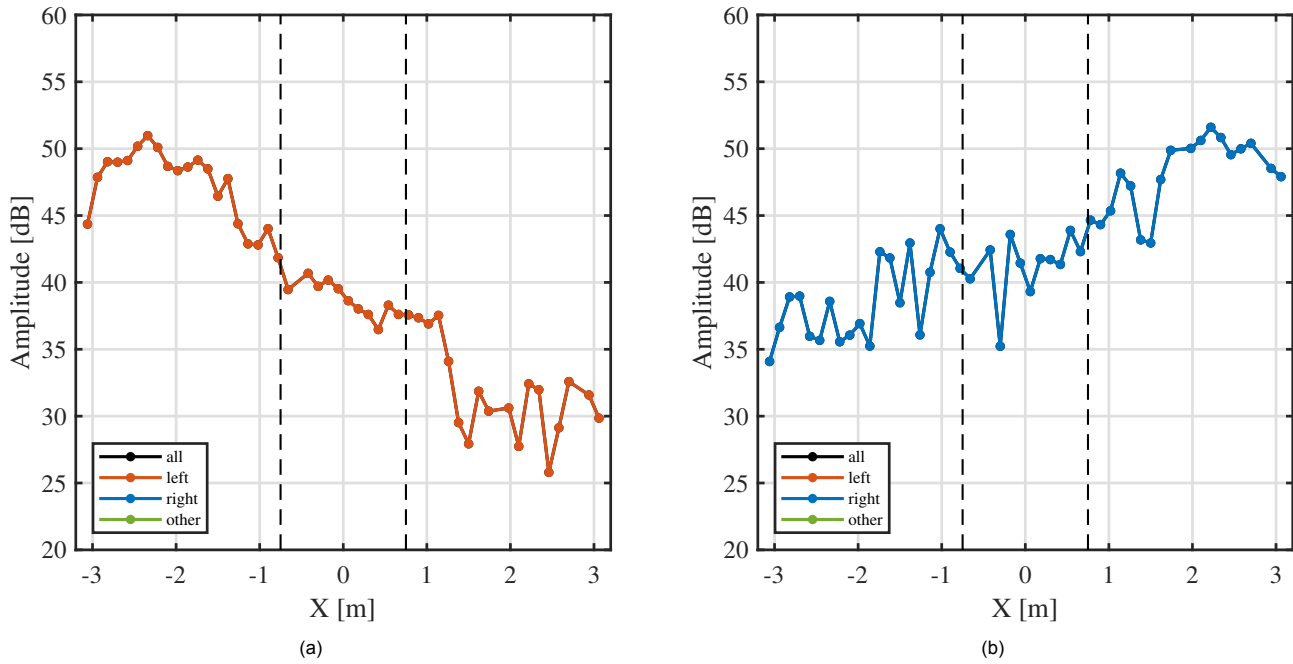
Figure 4.18: CLEAN-SC noise directivity breakdown for a one-third-octave frequency band centered at 3150 Hz for the big pipe with insulation foam and (a) the left speaker "on" and (b) the right speaker "on".

When investigating the directivity breakdown for the left speaker at 3150 Hz in Fig. 4.18a, the results are as expected, i.e. the *left* and the *all* lines coincide, indicating that there are no other visible contributions from other areas. The source map in Fig. 4.10b confirms that there are no other sources at 3150 Hz apart from those located at the left exit. Hence, CLEAN-SC is able to isolate the sources and their contributions for the simple single-source case. Moreover, the directivity breakdown shows most noise radiated on the left side, while, on the right side, the noise levels decrease. This makes sense as only the left speaker is turned on and the foam stops leakage through the pipe. Subsequently, in Fig. 4.18b, only the right speaker is turned on and the breakdown follows a similar pattern. There are only contributions from *right*, as confirmed by the source map in Fig. 4.12b. In this case, most noise is on the right side and the noise level decreases towards the left.
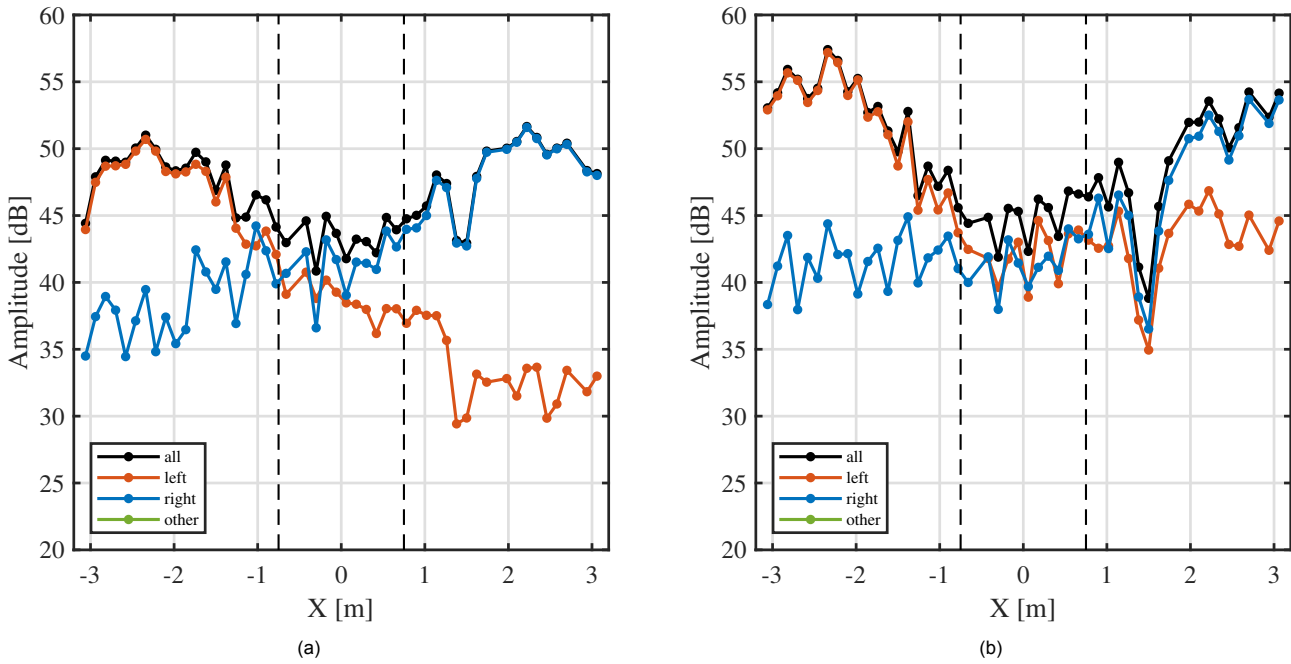
Figure 4.19: CLEAN-SC noise directivity breakdown for the big pipe with insulation foam and both speakers "on" for a one-third-octave frequency band centered at (a) 3150 Hz and (b) 5000 Hz.

The directivity breakdown can also be performed for the more challenging case with both speakers on. In Fig. 4.19 the breakdown for both speakers on is shown, where the breakdown in Fig. 4.19a corresponding to a one-third-octave-band centered at 3150 Hz and Fig. 4.19b is for 5000 Hz. The results for both frequency bands are as expected. CLEAN-SC is able to differentiate the sources and perform the directivity breakdown of these sources. On the left side, the left sources are dominant and on the right side, the right sources are dominant, while for the center section of the pipe, both speakers have an equal contribution to the total noise. Subsequently, as discussed earlier the right speaker outperforms the left speaker below 5000 Hz, which results in the sources on the right being a bit louder for 3150 Hz, while for 5000 Hz this is the other way around and the left speaker is louder. Another noticeable aspect in the breakdown for 5000 Hz, is that the microphones at X = 1.5 m and X = 1.38 m start to display an amplitude off-set compared to the microphones neighbour microphones, as discussed in subsection 4.1.2.

Now, the main goal of this study is to assess whether CLEAN-SC is capable of performing a precise directivity breakdown when multiple sources are present. Therefore, the breakdown of the case with just the left speaker on is compared (and used as a reference) to the breakdown of the left speaker with both speakers on. Essentially, Fig. 4.18a is compared to the contribution of left sources in Fig. 4.19a.

The comparison of the results is depicted in Fig. 4.20a. The case with one speaker on is represented by the blue line and functions as the baseline. The red line is the contribution of left noise sources when both speakers are on. Thus, by comparing the lines it can be determined if the directivity breakdown is still precise when another source is present. It can be observed that on the left side, the lines are almost identical, which means that the breakdown is considerably precise. However, on the right side, a larger deviation is observed between both results. This indicates that on the side where the other source is dominant, it is more difficult to separate the contribution of the left speaker from the noise of the right speaker, while for the section in the middle of the pipe, where neither the left nor the right speaker is dominant, the difference between the lines fluctuates between both cases. Subsequently, the difference in sound pressure level between both cases is plotted in Fig. 4.20b, where this pattern is visible. In this instance, a positive amplitude difference indicates that the baseline is lower than the case to which it is compared, while a negative difference indicates that the baseline is higher than the other case.
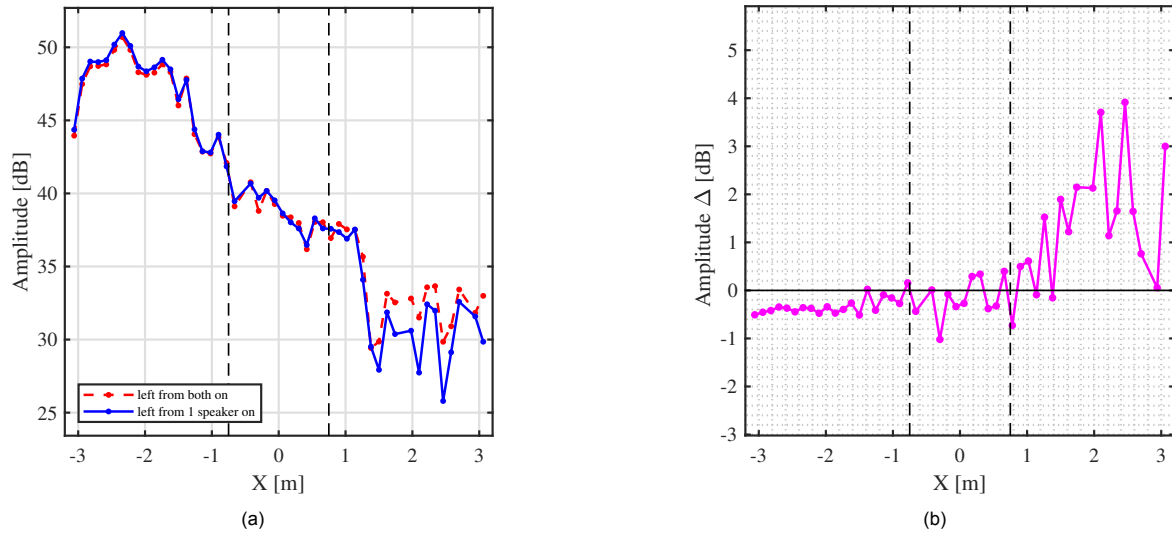
Figure 4.20: (a) Directivity breakdown comparison for a one-third-octave frequency band centered at 3150 Hz of the left speaker "on" to both speakers "on" for the big pipe with foam and (b) the amplitude difference between the cases.

Similar to the analysis on the left side, sources from the right source can also be compared, which is depicted in Fig. 4.21. In this case, results are shown for a one-third-octave band centered at 3150 Hz, for the right speaker on compared to the right side of both speakers on. A similar pattern is visible, where CLEAN-SC is again able to accurately break down the sources on the dominant side (the right side in this case). In the middle section of the pipe, the variations start to fluctuate more. While on the side where the right speaker is not dominant, the results deviate more from the baseline.

Furthermore, the directivity breakdown is also analysed for other frequency bands. The difference in amplitude of the breakdown of the left speaker on and the left side of both speakers is shown in Fig. 4.22a for a 1/3 octave band around 1000 Hz and in Fig. 4.22b for 5000 Hz. In these cases, the left side is the dominant side. Once again, it can be observed that for both cases the amplitude difference is small on the dominant side and that the amplitude difference increases on the non-dominant side. Additionally, the amplitude difference is larger at 5000 Hz, compared to the other two examples 1000 Hz or 3150 Hz.
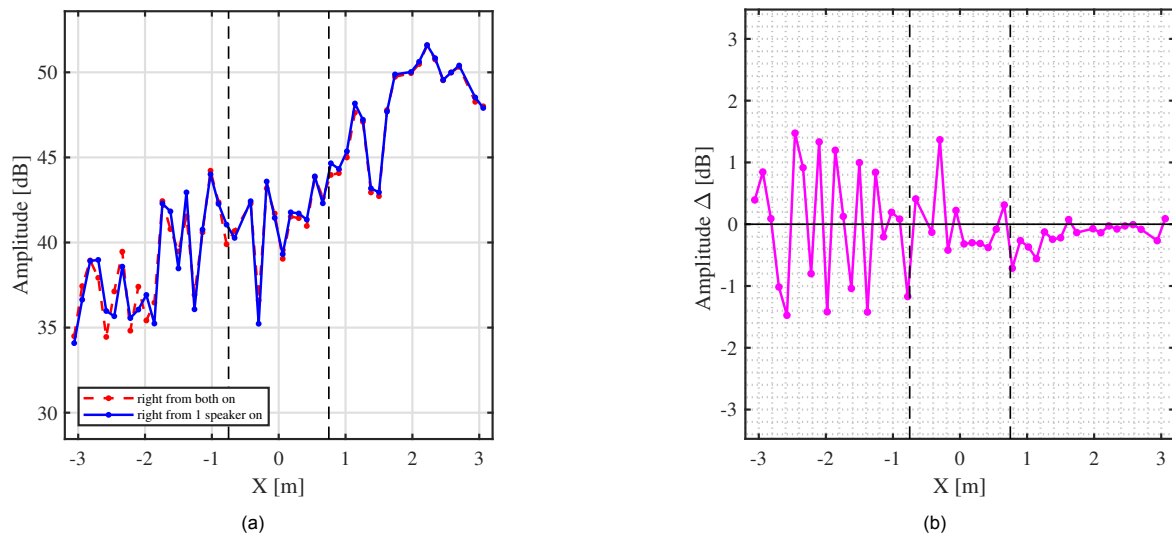

Figure 4.21: (a) Directivity breakdown comparison for a one-third-octave frequency band centered at 3150 Hz of the right speaker "on" to both speakers "on" for the big pipe with foam and (b) the amplitude difference between the cases.
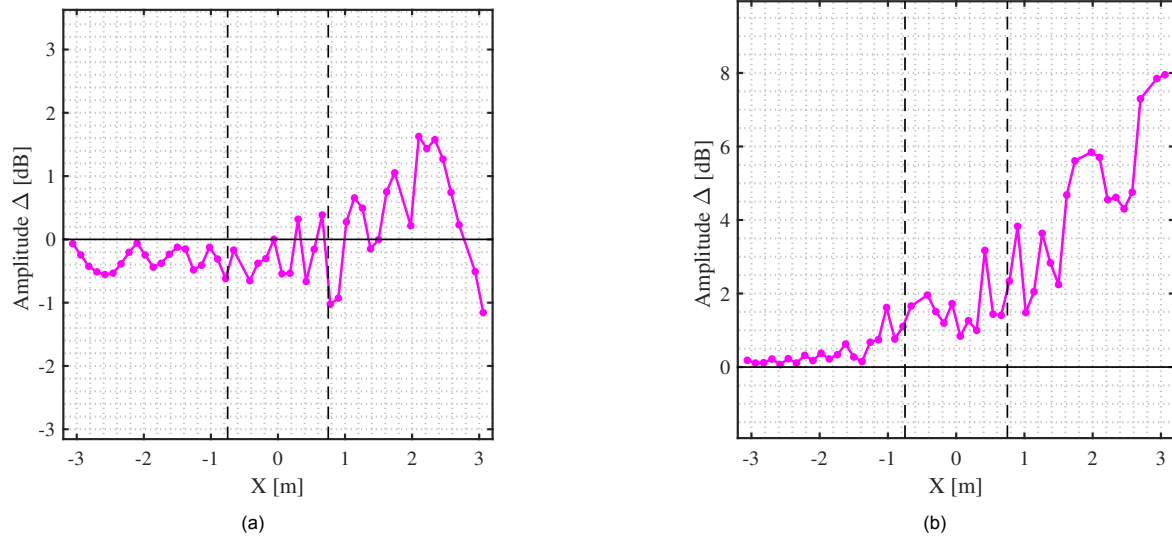
Figure 4.22: Amplitude difference of left speaker "on" compared to both speakers "on", for the big pipe with foam, for a one-third-octave frequency band centered at (a) 1000 Hz and (b) 5000 Hz.

So far the analysed directivity breakdowns came from experimental data, with both speakers set at a similar level, but tests have also been performed with the right speaker at a level 10 dB lower than the left speaker. For that case the breakdown is depicted in Fig. 4.23b. Subsequently, the baseline case with only the right speaker on, is shown in Fig. 4.23a. Now the same analysis can be applied and the difference between the sources on the right side from one speaker on can be compared to sources at the right side from both speakers on. Also the left side can be used for comparison. However, from the breakdown in Fig. 4.23b it can be determined that the left speaker dominates the spectrum over a larger part compared to a case, where both speakers are at the same level. As a result the precision of the directivity breakdown of the left side is expected to be better. On the other hand, since the right speaker has an even smaller contribution to the total noise on the left side, the precision is expected to be worse, especially for the left side. Hence it is more interesting to analyse the right side, as it is the more difficult test. The directivity breakdown comparison is shown in Fig. 4.24. The amplitude difference between one speaker on and both on is small on the right side of the pipe, which indicates that on that side the breakdown is precise. However, on the left side the amplitude difference between the baseline and both speakers on is large. This indicates that the breakdown is not as precise. This follows the same pattern as observed before, which is that if the analysed source only has a small contribution to the total noise, the precision of the breakdown decreases.
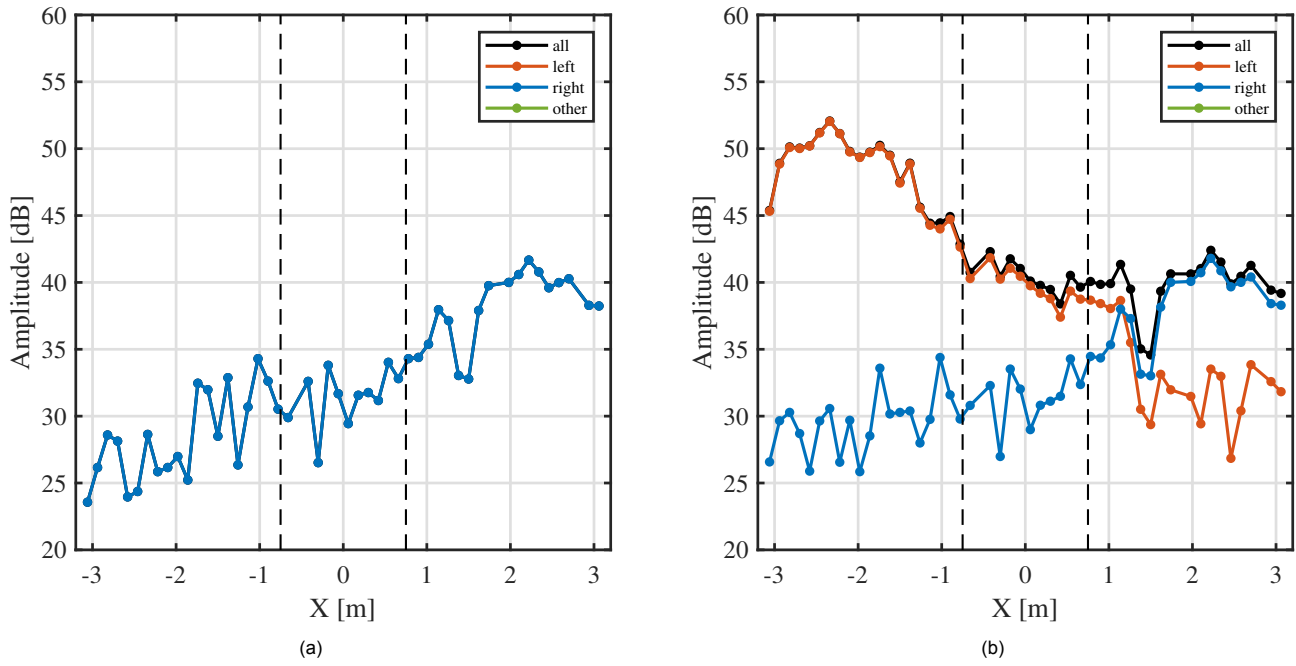
Figure 4.23: CLEAN-SC noise directivity breakdown for a one-third-octave frequency band centered at 3150 Hz for the big pipe with insulation foam and (a) the right speaker "on" at -10 dB and (b) both speakers "on", with the right speaker at 10 dB lower with respect to the left speaker
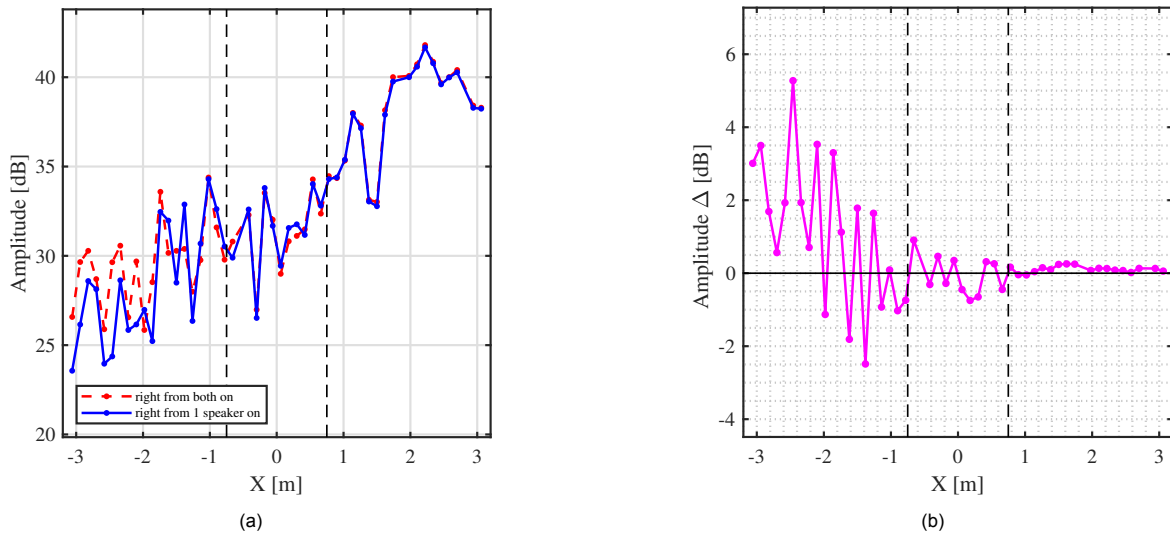

Figure 4.24: (a) Directivity breakdown comparison for a one-third-octave frequency band centered at 3150 Hz of the the right speaker "on" at -10 dB and both speakers "on", with the right speaker at 10 dB lower with respect to the left speaker and (b) the amplitude difference between the cases.

4.4. Detailed analysis of directivity breakdowns

In order to obtain a better overview of the performance of CLEAN-SC for multiple frequencies, the Root Mean Square (RMS) of the amplitude difference is computed for three separate sections; left, middle, and right. The sections are defined in Table 4.1, where the coordinates correspond to the locations of the microphones. By splitting the breakdown into sections, the different parts of the amplitude difference can be analysed separately. As discussed, the amplitude difference displays three regions of interest;

- The dominant side, where the analysed sources are the largest contributor to the total noise and the amplitude difference between the baseline and the same side from both speakers "on" is small.

- The middle, where the contribution of the analysed sources is equal to that of sources from the other side and the amplitude difference between the baseline and same side from both speakers "on" is increasing.

- The non-dominant side, where the analysed sources have a very small contribution to the total noise and the amplitude difference between the baseline and the same side from both speakers "on" is relatively high.

Note that the dominant side switches depending on which side is analysed. For example if sources on the right side are analysed, the dominant side is the right side, as these sources dominate the spectrum on the right side. While the left side is in that case the non-dominant side, because on the left side the right sources only have a small contribution to the total spectrum. On the other hand, if the left sources are analysed the left side is the dominant side and the right side becomes the non-dominant side.

The distinction between the dominant, middle and non-dominant side is made because, otherwise, the root mean square of the amplitude difference of the non-dominant side would dominate the total average, because the amplitude differences on the non-dominant side are significantly larger compared to the dominant side or the middle, despite being less relevant for the study.

The RMS indicates how much the amplitude differences between two cases deviate from zero (the ideal case). This RMS can be plotted for a range of frequencies and the overall breakdown capability of CLEAN-SC can be assessed per section over a frequency range. The RMS is computed using Eq. (4.2). $\Delta_N(f)$ is the difference between the red and the blue line for a certain frequency f and for a section, ranging from the locations in Table 4.1, where N indicates the microphone number. $N_{mic,sec}$ represents the number of microphones in a section.

Table 4.1: Sections considered for RMS-analysis. The X-coordinates and indices of the microphones, where the sections start and end.

Section	Start, X [m]	End, X [m]	$N_{mic,start}$	$N_{mic,end}$
Left	-3.06	-1.14	1	17
Middle	-1.02	1.02	18	34
Right	1.14	3.06	35	49

$$RMS(f) = \sqrt{\frac{1}{N_{mic,sec}} \sum_{N=N_{start}}^{N_{stop}} (\Delta_N(f))^2} \qquad (4.2)$$

The RMS plots of the amplitude difference in directivity breakdown between one speaker on and both speakers on for the big pipe with foam are shown in Fig. 4.25a for the left side and in Fig. 4.25b for the right side. When comparing the left side to the right side, two aspects stand out. Firstly, in the frequency range from 0.5 kHz to 3 kHz the RMS of all sections of the left side is larger than the right side, especially around 1.5 kHz to 2 kHz, where there is a significant increase. Secondly, the RMS of the non-dominant section is larger for the left side case.

Furthermore, the same RMS plots but for the small pipe are depicted in Fig. 4.26a for the left side and in Fig. 4.26b for the right side. When comparing left to right for the small pipe, there appear to be larger peaks in RMS values for the left side in the frequency range between 0.5 kHz to 3 kHz compared to the right side, which are similar findings as those from the big pipe analysis. Subsequently, on the right side, the RMS increases significantly at 4.5 kHz for the dominant section and the middle section.

The exact cause of the deviations in RMS is difficult to pinpoint, as there is a variety of factors that could play a role. The CLEAN-SC algorithm is not perfect as demonstrated by the deviation increase for the non-dominant section. The algorithm has lower precision when the analysed source becomes a smaller part of the total noise. One of the reasons for this decrease in precision is that the noise level scales logarithmically with the measured pressure. Therefore, the contribution of the analysed source is several scales lower compared to

the total measured noise. This can induces errors. In addition, the deviation can also be caused by speaker inconsistency, for example, it could be the case that the left speaker performs inconsistently between 1.5 kHz and 2 kHz, which leads to the larger deviation observed at that frequency. Another aspect that could play a role is some inconsistency in microphone performance or other small errors that can occur during the experiments. In general, the average RMS over the frequency range of all dominant sections is below 1 dB as listed in Table 4.2. This indicates that CLEAN-SC is able to break down the noise with high precision even when another sound source is present. Subsequently, for the middle section, where no single source is dominant, the results are more variable depending on the frequency. In general, the deviation is larger compared to the dominant side, however, the average RMS value is still relatively low. Therefore, it can be concluded that CLEAN-SC is able to perform a directivity breakdown when no dominant source is present with a relatively low error of around 1 dB in this case. Moreover, as discussed before, it can be observed that the RMS of the breakdown increases for the non-dominant section. Therefore, for the non-dominant side, it can be concluded that the breakdown is not as reliable, as for the dominant side.

It should also be noted that these results are obtained for an area of ± 0.15 with respect to the pipe exits. The selected area has a large effect on the RMS. For example, if the area is decreased some sources that are not located exactly on the pipe exit could fall under a different source area and, therefore, these sources will in that case contribute to the category of *other* instead. For this experiment there are no other sources present next to the speakers, hence it is possible to define the areas with some margin. Hence, for static engine testing, the source areas should be defined carefully to obtain the best results.

With regards to computation time, the additional cost of performing the directivity breakdown is low. As mentioned the CSM is split into contributions of the different source areas, which is performed simultaneously to generating the source maps. Therefore, it requires very little extra time. Even performing the RMS analysis, which requires the directivity breakdown for a large number of frequencies, can be done in a few minutes on a moderate laptop.

Table 4.2: Average values of the RMS for the different sections in dB per plot

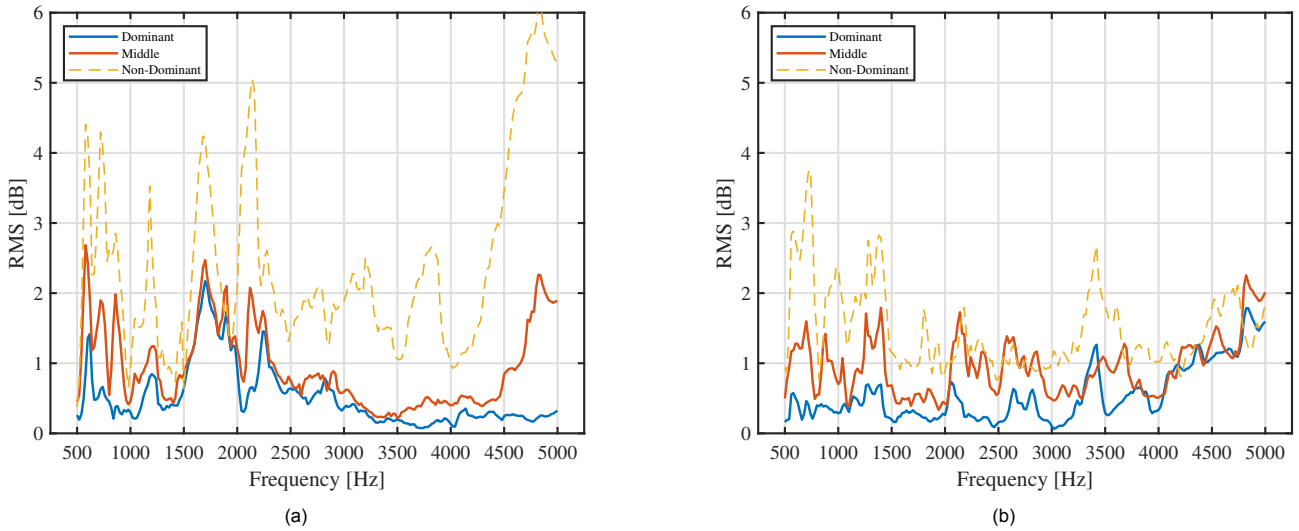| Section / RMS plot	Dominant	Middle	Non-Dominant
Big pipe left (Fig. 4.25a)	0.52	0.94	2.42
Big pipe right (Fig. 4.25b)	0.55	0.96	1.47
Small pipe left (Fig. 4.26a)	0.55	0.88	1.67
Small pipe right (Fig. 4.26b)	0.68	1.01	1.45
Average of all cases	0.58	0.95	1.75

Figure 4.25: RMS analysis results of the difference in directivity breakdown between one speaker "on" and both speakers "on" for the big pipe with foam for frequencies up to 5000 Hz for (a) the left speaker and (b) the right speaker.
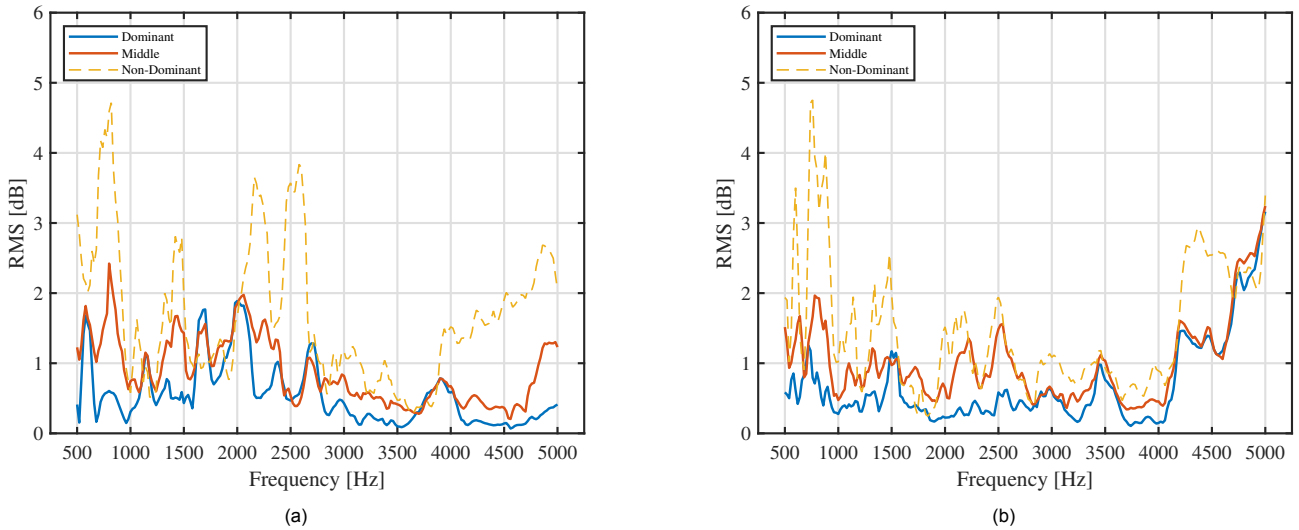

Figure 4.26: RMS analysis results of the difference in directivity breakdown between one speaker "on" and both speakers "on" for the small pipe with foam for frequencies up to 5000 Hz for (a) the left speaker and (b) the right speaker.

4.4.1. Normalized pressure instead of dB

The RMS plots and the amplitude plots have been expressed in dB, because this is the most common unit to express sound levels. Subsequently the directivity breakdown of other methods, such as SODIX, is also commonly expressed in dB [42]. Hence, it makes sense to express the precision of the directivity breakdown of CLEAN-SC in dB as well. However, using dB as a unit has a drawback. Namely, that it is a logarithmic scale, which suppresses the difference between two cases on the dominant side and exaggerates the difference on the non-dominant side. For example, if Fig. 4.20b, is expressed in Pa^2 instead of dB, the amplitude difference is largest on the dominant side, as shown in Fig. 4.27. This is because the total absolute sound pressure is significantly higher on the dominant side and as a consequence the absolute pressure difference between two cases is large, but in dB the difference is small. While on the non-dominant side, the opposite is visible. The total sound pressure is low and, therefore, the absolute difference in Pa^2 is also low, however in dB the difference is large.

Now, from this it could be determined that actually the CLEAN-SC breakdown is more precise on the non-

dominant side, since the absolute pressure difference between the breakdown of two cases is lowest. However, in that case you would underestimate the precision in dB for the dominant side, which is arguably more important for the overall breakdown capabilities. It shows that the results look different when analysing the absolute pressure difference instead of the relative pressure difference. Especially, when comparing the dominant side and the non-dominant side.

Another way to analyse the relative pressure difference is to normalize the difference of the two cases. One way to do this is to express the difference as a fraction of the total measured pressure in that point. So for example for the microphone at X = -1.98 m, the difference is around -2.1×10^{-6} Pa^2, which can be normalized by dividing it by the total measured pressure of the baseline, which is -2.6×10^{-5} Pa^2. This way the difference is expressed as a fraction of the total pressure of the baseline. The result is depicted in Fig.4.28. It is observable that the pattern is similar to plot in dB as shown in Fig. 4.20b. On the dominant side the difference is small compared to the total measured pressure while on the dominant side the difference is large even when compared to total measured pressure. This confirms the results in dB; the precision of the directivity breakdown decreases for the non dominant side. Similarly, a RMS analysis can be performed for the normalized pressure difference. The results are shown in Appendix B and are consistent with the results in dB. This makes sense as both units are in some way normalized. In the end the precision of CLEAN-SC should not change depending on the unit. It makes sense to express the precision in dB, because this is the most common unit for breakdowns. But the pressure difference plots give a better overview of the precision, when normalized pressure is used as unit, because this is more intuitive than dB.

(a)   (b)
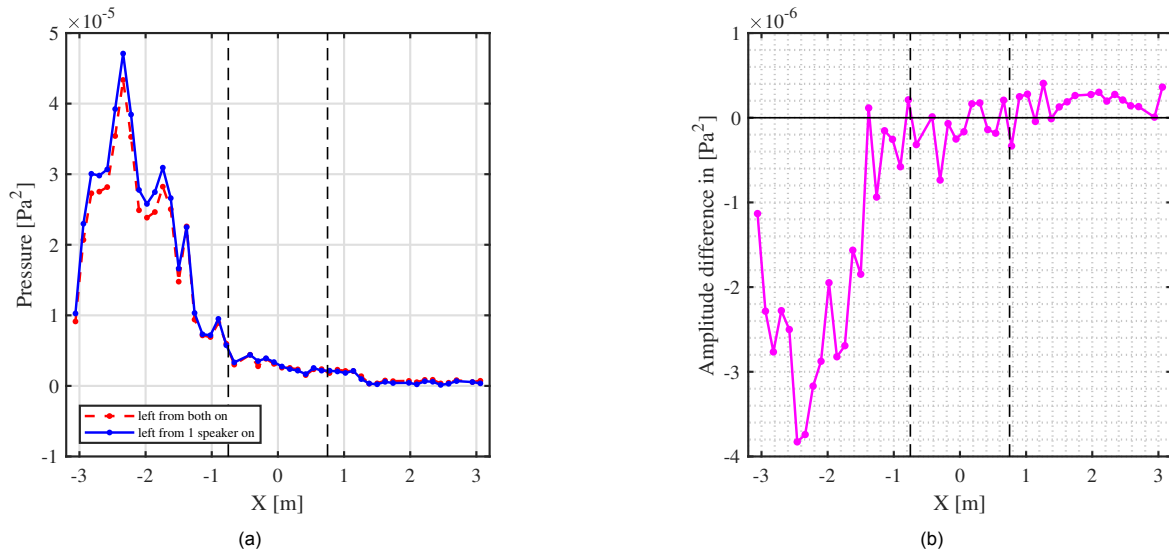
Figure 4.27: (a) Directivity breakdown comparison for a one-third-octave frequency band centered at 3150 Hz of the left speaker "on" to both speakers "on" for the big pipe with foam and (b) the amplitude difference in Pa^2 between the cases.
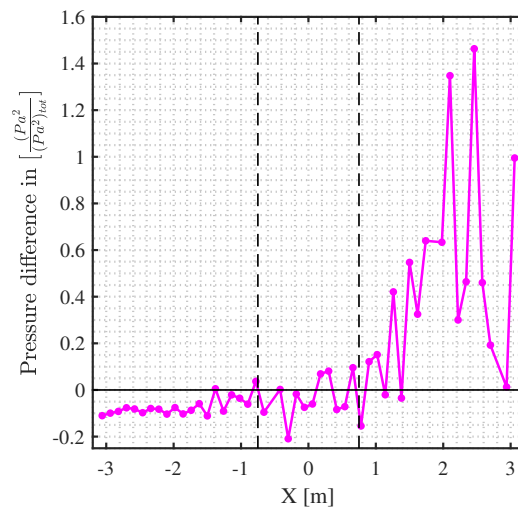
Figure 4.28: Directivity breakdown comparison for a one-third-octave frequency band centered at 3150 Hz of the left speaker "on" to both speakers "on" for the big pipe with foam and the normalized amplitude difference between the cases.

5

Conclusion

In conclusion, the goal of this study is to investigate the directivity breakdown capabilities of CLEAN-SC and to determine whether this method is capable of obtaining reliable directivity breakdowns from microphone data of measurements in the far field.

In order to investigate this, experimental data is obtained by performing a number of tests in the anechoic chamber at the faculty of Applied Sciences at Delft University of Technology. In these tests, the location and directivity of the sources are measured separately, so that the results can be compared to the outcome of the deconvolution tool CLEAN-SC. The data from the experiments is analysed by making acoustic source maps using CFDBF, DAMAS, and CLEAN-SC. In addition, CLEAN-SC is also used to perform a directivity breakdown of the data.

The breakdown of a case with one source is compared to a case with multiple sources. The comparison of both breakdowns for a one-third-octave frequency band centered at 3150 Hz, it is shown that CLEAN-SC is able to perform a proper breakdown even when another source is present. Especially, for the dominant side the difference between both cases is small. Meanwhile, on the side where the source is not dominant, the deviation increases. To analyse a large number of frequencies the Root Mean Square (RMS) of the difference is computed. This analysis shows that CLEAN-SC is able to perform a breakdown of the dominant section with only a small deviation of 0.5 dB for the frequency range between 500 Hz and 5000 Hz. The deviation for the middle sections where no single source is dominant is around 1 dB, but still sufficiently low for useful analysis. For the non-dominant sections, the deviation is around 2 dB, which makes analysis unreliable.

Based on the results of this study, CLEAN-SC should be able to reliably perform directivity breakdown of microphone data of static engine tests, especially for the areas where the noise of the analysed part is either the dominant source or one of the dominant sources.

Recommendations
Future work could include tests with more than two speakers at multiple different locations. This way, the effect of the number of sources, their proximity, and their location on the directivity breakdown could be analysed. Furthermore, it would be interesting to apply other methods, such as AFINDS or SODIX that can also perform directivity breakdown to the experimental data, so that the performance of these more computationally-expensive methods can be compared to CLEAN-SC.

Bibliography

[1] Pieter Sijtsma. *Acoustic beamforming for the ranking of aircraft noise*. 1st ed. VKI Lecture Series: Published in: Accurate and Efficient Aeroacoustic Prediction Approaches for Airframe Noise, 2013.

[2] Roberto Merino-Martinez et al. "Integration methods for distributed sound sources". In: *International Journal of Aeroacoustics* 18 (June 2019), p. 1475472X1985294. DOI: 10.1177/1475472X19852945.

[3] Roberto Merino Martinez. "Microphone arrays for imaging of aerospace noise sources". PhD thesis. Delft University of Technology, 2018. DOI: https://doi.org/10.4233/uuid:a3231ea9-1380-44f4-9a93-dbbd9a26f1d6.

[4] Pieter Sijtsma. "Using CLEAN-SC for determining the directivity of engine noise sources". In: *AIAA AVIATION 2023 Forum*. DOI: 10.2514/6.2023-3839. URL: https://arc.aiaa.org/doi/abs/10.2514/6.2023-3839.

[5] Sebastian Oertwig et al. "Extension of the source localization method SODIX for the determination of partially coherent sound sources". In: *28th AIAA/CEAS Aeroacoustics 2022 Conference*. DOI: 10.2514/6.2022-2812. URL: https://arc.aiaa.org/doi/abs/10.2514/6.2022-2812.

[6] Brian J. Tester et al. "Application of a noise source separation method (AFINDS) to external array measurements taken on short cowl engines in anechoic, outdoor, and indoor facilities". In: *28th AIAA/CEAS Aeroacoustics 2022 Conference*. DOI: 10.2514/6.2022-2811. URL: https://arc.aiaa.org/doi/abs/10.2514/6.2022-2811.

[7] Pieter Sijtsma. "CLEAN Based on Spatial Source Coherence". In: *International Journal of Aeroacoustics* 6.4 (2007), pp. 357–374. DOI: 10.1260/147547207783359459. URL: https://doi.org/10.1260/147547207783359459.

[8] *Airbus Global Market Forecast*. 2023. URL: https://www.airbus.com/en/products-services/commercial-aircraft/market/global-market-forecast.

[9] Xiaoqian Sun et al. "A data-driven analysis of the aviation recovery from the COVID-19 pandemic". In: *Journal of Air Transport Management* 109 (2023), p. 102401. DOI: https://doi.org/10.1016/j.jairtraman.2023.102401. URL: https://www.sciencedirect.com/science/article/pii/S0969699723000443.

[10] Eulalia Peris. *Environmental noise in Europe - 2020*. Tech. rep. European Environment Agency, 2020.

[11] Ayodele Adekunle Faiyetole et al. "The effects of aircraft noise on psychosocial health". In: *Journal of Transport & Health* 22 (2021), p. 101230. DOI: https://doi.org/10.1016/j.jth.2021.101230. URL: https://www.sciencedirect.com/science/article/pii/S2214140521002607.

[12] Mathias Basner et al. "WHO Environmental Noise Guidelines for the European Region: A Systematic Review on Environmental Noise and Effects on Sleep". In: *International Journal of Environmental Research and Public Health* 15.3 (2018). DOI: 10.3390/ijerph15030519. URL: https://www.mdpi.com/1660-4601/15/3/519.

[13] Directorate-General for Environment. *Zero pollution: New EU report calls for stronger action to reduce harmful noise pollution*. 2023. URL: https://environment.ec.europa.eu/news/zero-pollution-new-eu-report-calls-stronger-action-reduce-harmful-noise-pollution-2023-03-20_en (visited on 11/27/2023).

[14] Statista Research Department. *Number of flights performed by the global airline industry from 2004 to 2022, with a forecasts for 2023*. 2023. URL: https://www.statista.com/statistics/564769/airline-industry-number-of-flights/ (visited on 11/27/2023).

[15] Eberhard-Lothar Bertsch. "Noise Prediction within Conceptual Aircraft Design". PhD thesis. Deutsches Zentrum für Luft- und Raumfahrt Institut für Aerodynamik und Strömungstechnik, Braunschweig, 2013.

[16]   Oleksandr Zaporozhets et al. *Aircraft Noise Assesment, prediction and control*. 1st ed. New York: Spon Press, 2012.

[17]   Lars Enghardt. "Aeroacoustics research in Europe: The CEAS-ASC report on 2017 highlights". In: *Journal of Sound and Vibration* 450 (2019), pp. 175–198. DOI: https://doi.org/10.1016/j.jsv.2019.03.006. URL: https://www.sciencedirect.com/science/article/pii/S0022460X19301646.

[18]   Jeffrey J. Berton. "System Noise Prediction of the DGEN 380 Turbofan Engine". In: *Journal of Aircraft* 53.6 (2016), pp. 1779–1786. DOI: 10.2514/1.C033616. eprint: https://doi.org/10.2514/1.C033616. URL: https://doi.org/10.2514/1.C033616.

[19]   Roger Storm et al. "A NASA Guide to Engines". In: *NASA Glenn Research Center Office of Educational Programs* (2007).

[20]   KIRK SORENSEN. *A Brief History of the Liquid-Fluoride Reactor*. 2006. URL: https://energyfromthorium.com/2006/04/22/a-brief-history-of-the-liquid-fluoride-reactor/ (visited on 11/22/2023).

[21]   Isabel Henrich. *How does a turbofan engine work?* 2021. URL: https://aeroreport.de/en/good-to-know/how-does-a-turbofan-engine-work (visited on 11/22/2023).

[22]   K. Aainsqatsit. *Schematic diagram illustrating the operation of a 2-spool, high-bypass turbofan engine, with LP spool in green and HP spool in purple.* 2009. URL: https://commons.wikimedia.org/wiki/File:Turbofan_operation-fr.svg (visited on 12/13/2023).

[23]   Abhishek Kumar Sahai. "Consideration of Aircraft Noise Annoyance during Conceptual Aircraft Design". PhD thesis. Rheinisch–Westfälische Technische Hochschule Aachen, 2016.

[24]   Dennis L Huff. "Noise reduction technologies for turbofan engines". In: *35th International Congress and Exposition on Noise Control Engineering (INTER-NOISE 2006)*. E-15787. 2007.

[25]   Chitrarth Prasad et al. "A study of noise reduction mechanisms of jets with fluid inserts". In: *Journal of Sound and Vibration* 476 (2020), p. 115331. DOI: https://doi.org/10.1016/j.jsv.2020.115331. URL: https://www.sciencedirect.com/science/article/pii/S0022460X20301620.

[26]   M. J . Lighthill. "On sound generated aerodynamically I. General theory". In: *Proceedings of the Royal Society of London. Series A, Mathematical and Physical Sciences* 211.564 (1951). DOI: https://doi.org/10.1098/rspa.1952.0060.

[27]   Steven A.E. Miller. "Broadband shock-associated noise near-field cross-spectra". In: *Journal of Sound and Vibration* 372 (2016), pp. 82–104. DOI: https://doi.org/10.1016/j.jsv.2016.01.048. URL: https://www.sciencedirect.com/science/article/pii/S0022460X16000973.

[28]   Jim Banke. *NASA Helps Create a More Silent Night*. 2010. URL: https://www.nasa.gov/aeronautics/nasa-helps-create-a-more-silent-night/ (visited on 12/13/2023).

[29]   Xiran Liu et al. "Development and progress in aeroacoustic noise reduction on turbofan aeroengines". In: *Progress in Aerospace Sciences* 130 (2022), p. 100796. DOI: https://doi.org/10.1016/j.paerosci.2021.100796.

[30]   Lars Enghardt. DLR Berlin. *PROBAND: Improvement of Fan Broadband Noise Prediction: Experimental investigation and computational modelling*. 2008. URL: https://www.win.tue.nl/ceas-asc/Workshop12/Bilbao-2008-Lars-Enghardt.pdf.

[31]   Marcus F. Heidmann. *Interim Prediction Method for Fan and Compressor Source Noise*. Tech. rep. NASA, 1979.

[32]   Nigel Peake et al. "Modern Challenges Facing Turbomachinery Aeroacoustics". In: *Annual Review of Fluid Mechanics* 44.1 (2012), pp. 227–248. DOI: 10.1146/annurev-fluid-120710-101231. URL: https://doi.org/10.1146/annurev-fluid-120710-101231.

[33]   A. Wohlbrandt et al. "Impact of cyclostationarity on fan broadband noise prediction". In: *Journal of Sound and Vibration* 420 (2018), pp. 142–164. DOI: https://doi.org/10.1016/j.jsv.2018.01.039.

[34]   J. E. Ffowcs Williams et al. "Aerodynamic sound generation by turbulent flow in the vicinity of a scattering half plane". In: *Journal of Fluid Mechanics* 40.4 (1970), pp. 657–670. DOI: 10.1017/S0022112070000368.

[35] Matthew Paul Allen. "Analysis and Synthesis of Aicraft Engine Fan Noise for Use in Psychoacoustic Studies". PhD thesis. Virginia Tech, 2012.

[36] Visaton – Speaker K 50 SQ – 8 Ohm. *http://www.visaton.de/en/products/fullrange-systems/k-50-sq-8-ohm*. English. Accessed in March 2017. URL: http://www.visaton.de/en/products/fullrange-systems/k-50-sq-8-ohm.

[37] Sjoerd W. Rienstra. *Fundamentals of Duct Acoustics*. Technische Universiteit Eindhoven, 2015.

[38] Thomas F. Brooks et al. "A deconvolution approach for the mapping of acoustic sources (DAMAS) determined from phased microphone arrays". In: *Journal of Sound and Vibration* 294.4 (2006), pp. 856–879. DOI: https://doi.org/10.1016/j.jsv.2005.12.046. URL: https://www.sciencedirect.com/science/article/pii/S0022460X06000289.

[39] Ennes Sarradj. "Three-Dimensional Acoustic Source Mapping with Different Beamforming Steering Vector Formulations". In: *Advances in Acoustics and Vibration* 2012 (2012), p. 12. DOI: https://doi.org/10.1155/2012/292695.

[40] Thomas Ahlefeldt et al. "A Tomographic Directivity Approach to Frequency Domain Beamforming". In: *2018 AIAA/CEAS Aeroacoustics Conference*. DOI: 10.2514/6.2018-2808. eprint: https://arc.aiaa.org/doi/pdf/10.2514/6.2018-2808. URL: https://arc.aiaa.org/doi/abs/10.2514/6.2018-2808.

[41] Stewart Glegg et al. *Aeroacoustics of Low Mach Number Flows*. Elsevier Inc., 2017.

[42] Sebastian Oertwig et al. "Quantifying the Effect of an Acoustic Liner from Far-Field Measurements in Static Engine Noise Tests". In: *eForum Acusticum 2020*. Lyon, France, Dec. 2020, pp. 353–357. DOI: 10.48465/fa.2020.0719. URL: https://hal.science/hal-03229458.

A
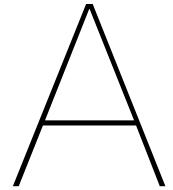
Test Matrix

Table A.1: Full Test Matrix

meas nr.	left	right	duration
Big Pipe, No foam			
1 background	off	off	10
2	on	off	30
3	off	on	30
4	off	-4	30
5	off	-10	30
6	on	on	30
7	on	-4	30
8	on	-10	30
9 tap test	off	off	10
Insert foam			
10	on	off	30
11	off	on	30
12	off	-6	30
13	off	-12	30
14	on	on	30
15	on	-6	30
16	on	-12	30
17 tap test	off	off	10
Small pipe, no foam			
18	on	off	30
19	off	on	30
20	off	-6	30
21	off	-12	30
22	on	on	30
23	on	-6	30
24	on	-12	30
25 tap test	off	off	10
Insert foam			
26	on	off	30
27	off	on	30
28	off	-6	30
29	off	-12	30
30	on	on	30
31	on	-6	30
32	on	-12	30
33 tap test,	off	off	10
Extra tests			
34 No pipe, speakers at exit	on	off	10
35	off	on	10
36	on	on	10
37 speaker at left side of the array			10
38 speaker at right side of the array			10

B

RMS analysis for the normalized pressure

Similarly to the RMS analysis in dB the same analysis can be performed using the normalized pressure. In Fig. B.1 the results of the big pipe are shown and in Fig. B.2 of the small pipe. Subsequently, the average RMS values are given in Table B.1. The results in normalized pressure are consistent with the results in dB. The largest difference is observed on the non dominant side and the lowest difference is observed for the dominant side.

Table B.1: Average values of the RMS for the different sections in normalized pressure per plot

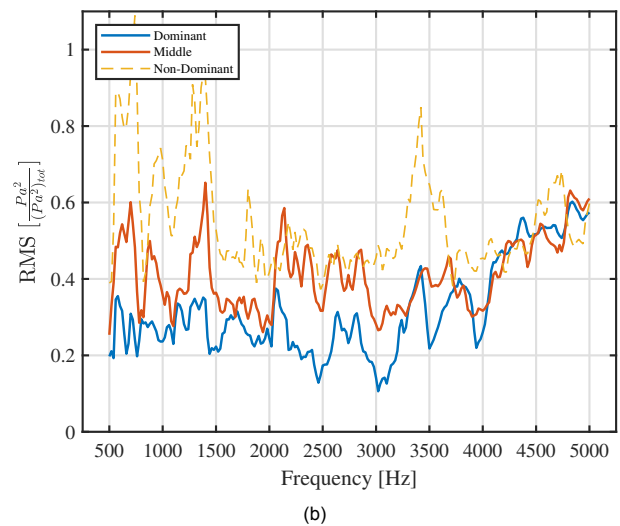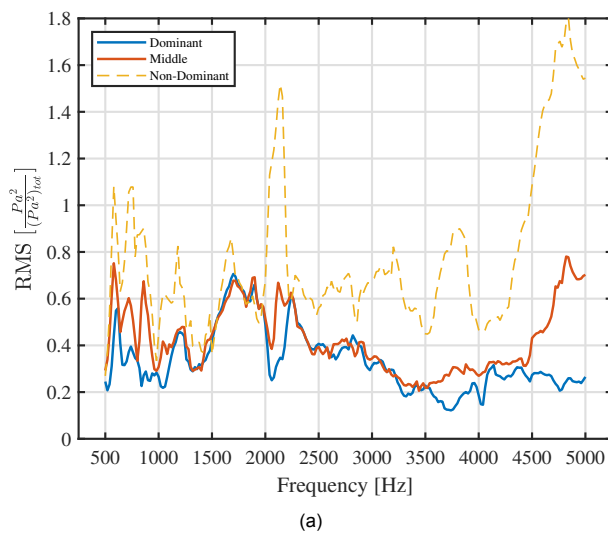| Section / RMS plot	Dominant	Middle	Non-Dominant
Big pipe left (Fig. B.1a)	0.33	0.43	0.77
Big pipe right (Fig. B.1b)	0.32	0.41	0.55
Small pipe left (Fig. B.2a)	0.30	0.39	0.58
Small pipe right (Fig. B.2b)	0.33	0.42	0.51
Average of all cases	0.32	0.41	0.60

(a)　　　　　　　　　　　　　　(b)

Figure B.1: RMS analysis results of the normalized pressure in directivity breakdown between one speaker on and both speakers on for the big pipe with foam for frequencies up to 5000 Hz for (a) the left speaker and (b) the right speaker.
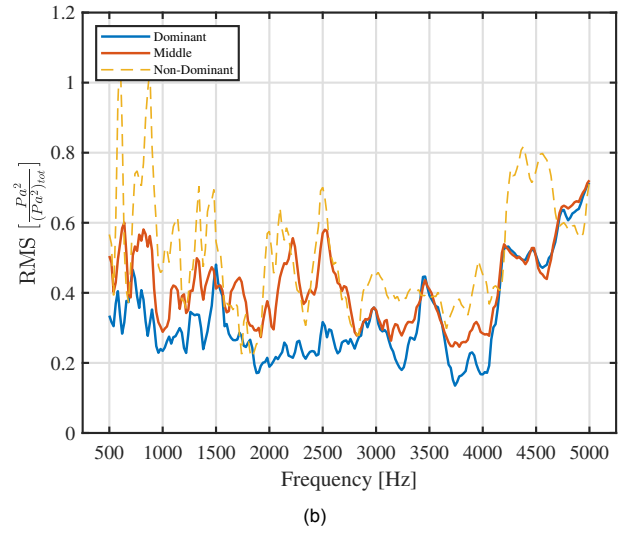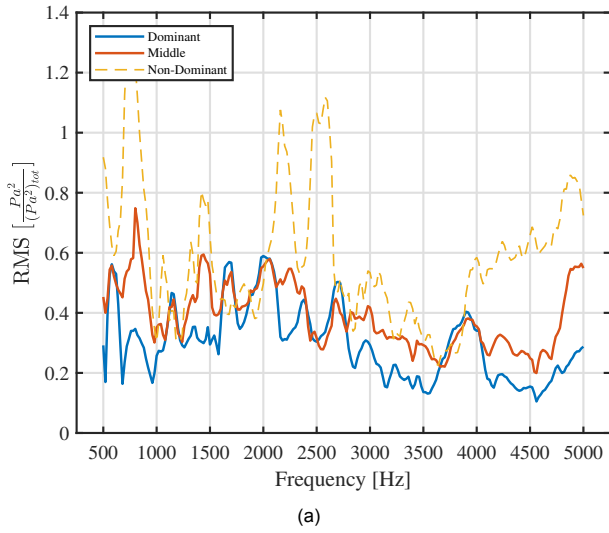
Figure B.2: RMS analysis results of the normalized pressure difference in directivity breakdown between one speaker on and both speakers on for the small pipe with foam for frequencies up to 5000 Hz for (a) the left speaker and (b) the right speaker.